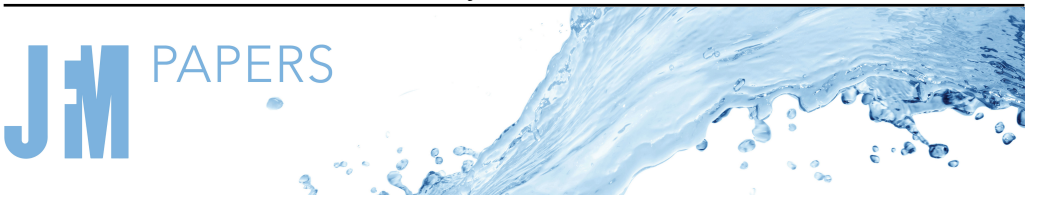
J. Fluid Mech. (2026), *vol.* 1043, A39, doi:10.1017/jfm.2026.11984



Instability of thin-film flows with temperature-dependent viscosity

Nicolas Morales-Preciado[1], **Neil J. Balmforth**[1] and **Christian Schoof**[1,2]

[1]Department of Mathematics, University of British Columbia, Vancouver, BC V6T 1Z2, Canada

[2]Department of Earth, Atmosphere & Ocean Sciences, University of British Columbia, Vancouver, BC V6T 1Z2, Canada

Corresponding author: Nicolas Morales-Preciado, nicolasmp95@math.ubc.ca

(Received 12 November 2025 UTC; revised 12 July 2026 UTC; accepted 16 July 2026 UTC)

We explore thermo-viscous instabilities in an idealised setting motivated by ice-sheet flow, modelled as a shallow layer of fluid with a temperature-dependent viscosity flowing down an inclined plane and subject to a constant geothermal heat flux. In this setting, multiple steady states are possible for a given slope, and we examine their linear stability to general wave-like perturbations in both the streamwise and transverse directions. We confirm that the lower and upper branches are stable with respect to perturbations that are spatially uniform in the two horizontal directions, but the intermediate state is unstable. For finite-wavenumber perturbations and with heat diffusion into the underlying bedrock, we find that all three branches are unstable. The lower and upper branches exhibit a relatively weak instability with respect to waves with finite streamwise wavelength and long transverse wavelengths, caused by diffusion of heat into the bedrock. Across all branches, the strongest instability occurs when the transverse wavelength is infinite and streamwise wavelengths are order one. Along the intermediate branch, modes remain unstable for all transverse wavenumbers, and growth rates do not decay in the limit of short transverse wavelengths. Motivated by this observation, we also briefly examine a simplified nonlinear problem for transverse perturbations, in order to clarify the implications of this missing short-wavelength cutoff.

Key words: thin films, ice sheets, gravity currents

1. Introduction

The creeping motion of glaciers is often modelled as the slow, shallow flow of a non-Newtonian fluid analogous to classical models of viscous gravity currents (Hutter 1983;

© The Author(s), 2026. Published by Cambridge University Press. This is an Open Access article, distributed under the terms of the Creative Commons Attribution licence (https://creativecommons.org/licenses/by/4.0/), which permits unrestricted re-use, distribution and reproduction, provided the original article is properly cited.

https://doi.org/10.1017/jfm.2026.11984 Published online by Cambridge University Press

Schoof & Hewitt 2013). A complication arises, however, due to the coupling between the relatively slow diffusion of heat across the ice thickness, viscous dissipation and a strongly temperature-dependent rheology. This coupling opens up the possibility that creeping flows can suffer thermo-viscous instabilities. Early studies focused mainly on streamwise instabilities in glacier and ice-sheet models (Clarke *et al.* 1977; Yuen & Schubert 1979; Fowler 1980; Fowler & Larson 1980), while later work extended the analysis to three-dimensional models and considered the possibility of transverse instabilities (Payne & Baldwin 2000; Hindmarsh 2004).

A typical explanation of the origin of such instabilities is that they arise because of thermal runaway: in simple flows down inclined planes, a slight warming causes a lower viscosity, accelerating flow and increasing viscous dissipation, which then heats up the ice further. Many authors have analysed thermo-viscous instability by examining how the flux of steady base-flow states depends on the parameters of the problem, such as the inclination of the underlying plane. In particular, the flux can be a non-monotonic function of the slope, implying that multiple solutions can occur for the same parameter settings. This suggests a loss of stability at the (saddle-node) bifurcations, where the solution folds back upon itself, in the same manner that instability is thought to be associated with multiple solutions in a great many other problems.

Nevertheless, as noted by Maddocks (1987), it may not be possible to determine stability alone from the folds on a bifurcation diagram of the steady states. Instabilities can arise that cannot be categorised in this way, owing to richer spatial structure or time-dependent dynamics. Indeed, for ice flow, Hindmarsh (2004) has previously noted that linear instabilities can occur on both sides of the folds on the steady-state flux curve. In addition, and more problematically, Hindmarsh also notes that shallow-ice models can predict instabilities at arbitrarily large wavenumbers, with no apparent decay of growth rates in that limit.

Traditionally, shallow-ice models offer a simplified and computationally efficient means to describe the dynamics of glaciers. However, the possibility that these models cannot adequately capture the essential physics calls into question their usage. Numerical experiments with shallow-ice models have previously demonstrated problematic dependence on grid resolution (Payne & Baldwin 2000), which may be the manifestation of Hindmarsh's observation of instability at arbitrarily short wavelengths, and has led to the widespread adoption of more complex, 'higher-order' models for shallow-ice flow (Schoof & Hindmarsh 2010). This motivates us to investigate the break down of the shallow-ice approximation, focusing on analytical results to complement the purely numerical stability analysis in Hindmarsh (2004).

We provide a detailed study of the flow of a sheet of ice over an inclined plane. We adopt the shallow-ice approximation, treating the ice as a temperature-dependent, non-Newtonian fluid. In particular, following common practice, we assume that ice is a shear-thinning fluid, with an effective viscosity that depends on temperature through an Arrhenius relation. We also deliberately ignore sliding at the base of the ice, which is often regarded as an essential part in the dynamics of ice streams (Kyrke-Smith *et al.* 2014; Schoof & Mantelli 2021). These finger-like regions of highly elevated ice velocities within an ice sheet (Alley & Bindschadler 2001) are likely to be an end member in the evolution of thermomechanical instabilities, and generally correspond to the temperature at the base of the ice having reached the melting point. Pattern-forming instabilities can, however, occur at lower temperatures, and by isolating thermoviscous feedbacks in the absence of sliding, we are able to provide a clearer analysis. This approach complements previous numerical studies (Payne & Baldwin 2000; Payne *et al.* 2000; Hindmarsh 2004; Saito *et al.* 2006) by helping to identify the physical mechanisms responsible for the

https://doi.org/10.1017/jfm.2026.11984 Published online by Cambridge University Press

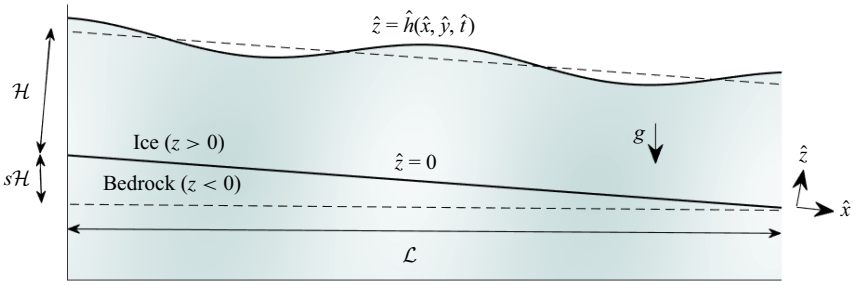


Figure 1. Sketch of the model geometry. Cartesian coordinates are aligned with an inclined plane corresponding to the ice–rock interface. The shading represents temperature perturbations in both the ice and bedrock.

instability and the conditions under which the shallow-ice approximation ceases to be reliable, while also allowing us to explore the dynamics along each branch of the flux curve.

Our study is organised as follows: in § 2, we outline the shallow-ice model. Section 3 investigates steady flows, and constructs steady-state flux curves. In § 4, we analyse the two-dimensional and three-dimensional linear stability of the system, starting with perturbations that depend only on height above the ice–bedrock interface in § 4.1, then introduce structure in the streamwise (§ 4.2) and transverse (§ 4.3) directions, before briefly exploring a restricted version of the nonlinear problem for transverse perturbations in § 4.4. In the final § 5, we summarise and discuss our findings.

2. The model

2.1. *Formulation*

In this study, we employ a model closely related to that in Hindmarsh (2004), to describe ice flow over an infinite sloped plane, except that we neglect basal sliding and assume no surface accumulation. The geometry is described by a Cartesian coordinate system, $(\hat{x}, \hat{y}, \hat{z})$, where the $\hat{z}$-axis is perpendicular to the plane and the $\hat{x}$-axis aligns with the flow direction. The bedrock surface is flat, so that the lower boundary of the ice is $\hat{z} = 0$, and $\hat{h}(\hat{x}, \hat{y}, \hat{t})$ represents the ice thickness. The ice layer is shallow, with typical depths $\mathcal{H}$ much less than the characteristic length scale $\mathcal{L}$ for variations in the plane of the ice; the aspect ratio $\varepsilon = \mathcal{H}/\mathcal{L} \ll 1$. We assume further that the bedrock slope is small, of the same order of magnitude as the aspect ratio, and therefore define a scaled slope s such that εs is the actual slope; see figure 1. Note that we identify dimensional variables with hats, removing this decoration below when we switch to dimensionless variables.

This choice of scaling ensures that both the surface slope and the bedrock slope contribute to the leading-order momentum balance, as shown later, and therefore preserves the analogy with ice-sheet flow in an idealised flow-down-a-slope setting. We use this setting as a simplification of more realistic geophysically relevant flow geometries. In a more realistic model, one would generally include accumulation or ablation, allow the geometry and steady state to vary in the streamwise direction and determine the thickness together with the flow through mass conservation and appropriate upstream and downstream boundary conditions. Our aim here is not to model any particular glacier or ice sheet directly, but to isolate the thermomechanical effects in a simpler setting.

https://doi.org/10.1017/jfm.2026.11984 Published online by Cambridge University Press

The ice is modelled as an inertialess, incompressible fluid, so that

$$\boldsymbol{\nabla}\cdot\hat{\boldsymbol{\tau}} - \boldsymbol{\nabla}\hat{p} + \rho\boldsymbol{g} = \boldsymbol{0}, \tag{2.1}$$

$$\boldsymbol{\nabla}\cdot\hat{\boldsymbol{u}} = 0, \tag{2.2}$$

for $0 < \hat{z} < \hat{h}$, where $\hat{p}$ is the pressure, $\hat{\boldsymbol{\tau}}$ is the deviatoric stress tensor, ρ is the ice density and $\hat{\boldsymbol{u}} = (\hat{u}, \hat{v}, \hat{w})$ is the velocity field. The force of gravity vector is

$$\boldsymbol{g} = \frac{g}{\sqrt{1+\varepsilon^2 s^2}}\begin{pmatrix}\varepsilon s\\ -1\end{pmatrix}, \tag{2.3}$$

where g is gravitational acceleration.

The heat equation for the ice combines the effects of advection, diffusion and viscous dissipation, and can be written as

$$\hat{T}_{\hat{t}} + \hat{\boldsymbol{u}}\cdot\boldsymbol{\nabla}\hat{T} = \kappa_I\nabla^2\hat{T} + \frac{1}{\rho c_p}\hat{\boldsymbol{\tau}}:\hat{\boldsymbol{D}} \quad (0<\hat{z}<\hat{h}). \tag{2.4}$$

Here, $\hat{T}$ is the temperature, κ_I and c_p are the thermal diffusivity and heat capacity of ice, respectively, and $\hat{\boldsymbol{D}} = (\boldsymbol{\nabla}\hat{\boldsymbol{u}} + (\boldsymbol{\nabla}\hat{\boldsymbol{u}})^{\mathsf{T}})/2$ is the strain-rate tensor. We also use subscripts of $\{\hat{t}, \hat{x}, \hat{y}, \hat{z}\}$ to denote partial derivatives. In the bedrock, the absence of advection simplifies the heat equation to

$$\hat{T}_{\hat{t}} = \kappa_R\nabla^2\hat{T} \quad (\hat{z}<0), \tag{2.5}$$

where we use a subscript R rather than I to differentiate the material properties of the bedrock from those of the ice.

The ice surface is stress free and held at fixed temperature, assuming an instantaneous relaxation to a constant atmospheric temperature T_a. In combination with the kinematic condition, we impose

$$\left.\begin{aligned}\hat{\boldsymbol{\tau}}\cdot\boldsymbol{n} - \hat{p}\,\boldsymbol{n} &= \boldsymbol{0}\\ \hat{T} &= T_a\\ \hat{h}_{\hat{t}} + \hat{u}\hat{h}_{\hat{x}} + \hat{v}\hat{h}_{\hat{y}} &= \hat{w}\end{aligned}\right\} \quad \text{at } \hat{z} = \hat{h}, \tag{2.6}$$

where $\boldsymbol{n}$ is the outward unit vector normal to the surface. At the ice–bedrock interface, we impose no slip and the continuity of the temperature and heat flux, stated as

$$\left.\begin{aligned}\hat{\boldsymbol{u}} &= \boldsymbol{0}\\ \hat{T}^- &= \hat{T}^+\\ K_R\hat{T}^-_{\hat{z}} &= K_I\hat{T}^+_{\hat{z}}\end{aligned}\right\} \quad \text{on } \hat{z} = 0, \tag{2.7}$$

where K_I and K_R denote the thermal conductivities of ice and rock, and the $\pm$ superscripts denote the limits approached from above (the ice layer) or below (the bedrock), respectively. The no-slip assumption is unrealistic, as basal sliding would occur when temperatures approach the melting point. However, to isolate the effect of temperature-dependent viscosity, we neglect basal sliding. Deep within the bedrock, we prescribe a geothermal heat flux G, so that

$$-K_R\hat{T}_{\hat{z}} \to G, \quad \text{for} \quad \hat{z}\to-\infty. \tag{2.8}$$

To complete the model, we require a constitutive law relating strain rate $\hat{\boldsymbol{D}}$ to stress $\hat{\boldsymbol{\tau}}$. We adopt a generalised Newtonian fluid model, in which the effective viscosity is a function of both temperature and stress, so that

https://doi.org/10.1017/jfm.2026.11984 Published online by Cambridge University Press

$$\hat{\boldsymbol{D}} = \hat{f}(\hat{\tau}, \hat{T})\frac{\hat{\boldsymbol{\tau}}}{\hat{\tau}}, \quad \hat{\tau}^2 = \frac{1}{2}\hat{\boldsymbol{\tau}} : \hat{\boldsymbol{\tau}}. \tag{2.9}$$

2.2. *Non-dimensionalisation*

Following the usual shallow-ice approximation (Fowler & Larson 1978; Hutter 1983), we define scaled variables as

$$(x, y) = \frac{(\hat{x}, \hat{y})}{\mathcal{L}}, \quad (z, h) = \frac{(\hat{z}, \hat{h})}{\mathcal{H}}, \quad (u, v) = \frac{(\hat{u}, \hat{v})}{\mathcal{U}}, \quad w = \frac{\hat{w}}{\varepsilon\mathcal{U}}, \quad t = \frac{\mathcal{U}\hat{t}}{\mathcal{L}}, \tag{2.10}$$

$$(p, \varepsilon\boldsymbol{\tau}) = \frac{(\hat{p}, \hat{\boldsymbol{\tau}})}{\rho g\mathcal{H}}, \quad f(\tau, T) = \frac{\hat{f}(\hat{\tau}, \hat{T})}{\hat{f}(\varepsilon\rho g\mathcal{H}, T_a)}, \quad T = \frac{\hat{T} - T_a}{[\Delta T]}, \tag{2.11}$$

where

$$[\Delta T] = \left(\frac{1}{\hat{f}}\frac{\partial \hat{f}}{\partial \hat{T}}\right)^{-1}\Bigg|_{\{\hat{\tau}=\varepsilon\rho g\mathcal{H}, \hat{T}=T_a\}}, \quad \mathcal{H} = \frac{c_p[\Delta T]}{g}, \quad \mathcal{U} = 2\mathcal{H}\hat{f}(\varepsilon\rho g\mathcal{H}, T_a), \quad \mathcal{L} = \frac{\mathcal{H}^2\mathcal{U}}{\kappa_I}. \tag{2.12}$$

Through (2.12), we define scales for $\hat{T} - T_a$ and $\hat{f}$ from the shear rate and its sensitivity to temperature, evaluated at the characteristic shear stress $\varepsilon\rho g\mathcal{H}$ and atmospheric temperate T_a. The remaining characteristic scales, $\mathcal{H}$, $\mathcal{L}$ and $\mathcal{U}$ are chosen to ensure unit Brinkmann and Péclet numbers. Thus, $\mathcal{H}$ and $\mathcal{L}$ are determined by the material parameters and thermo-mechanical balances in the governing equations, rather than from geometric features of a particular ice sheet. Although this is not the standard scaling in glacier modelling, it is analytically convenient because it retains advection, diffusion and viscous heating at leading order while reducing the number of control parameters.

To leading order in ε, the pressure is hydrostatic, $p = h - z$. Substituting into the momentum equations in the x and y-directions, integrating with respect to z and applying the stress-free boundary condition at the surface, we obtain

$$\boldsymbol{\tau} = \begin{pmatrix}\tau_{13}\\ \tau_{23}\end{pmatrix} = (h - z)\begin{pmatrix}s - h_x\\ -h_y\end{pmatrix}. \tag{2.13}$$

The remaining leading-order system is given by

$$u_x + v_y + w_z = 0, \tag{2.14}$$

$$T_t + uT_x + vT_y + wT_z = T_{zz} + \tau f(\tau, T), \tag{2.15}$$

$$\begin{pmatrix}u_z\\ v_z\end{pmatrix} = f(\tau, T)\frac{\boldsymbol{\tau}}{\tau}, \quad \tau = \sqrt{\tau_{13}^2 + \tau_{23}^2}, \tag{2.16}$$

for $0 < z < h$, and

$$T_t = \kappa T_{zz}, \quad \kappa = \frac{\kappa_R}{\kappa_I}, \tag{2.17}$$

for $z < 0$. The boundary conditions become

$$h_t + uh_x + vh_y = w, \quad T = 0, \quad \text{at } z = h, \tag{2.18}$$

https://doi.org/10.1017/jfm.2026.11984 Published online by Cambridge University Press

$$T^- = T^+, \quad KT_z^- = T_z^+, \quad \boldsymbol{u} = \boldsymbol{0}, \quad \text{at } z = 0, \tag{2.19}$$

and

$$T_z \to -\Gamma/K, \quad \text{for } z \to -\infty, \tag{2.20}$$

where

$$\Gamma = \frac{\mathcal{H}G}{[\Delta T]K_I} \quad \text{and} \quad K = \frac{K_R}{K_I} \tag{2.21}$$

are the dimensionless geothermal flux and thermal conductivity ratio.

Moreover, the depth-integrated form of mass conservation, which determines the evolution of ice thickness, is

$$h_t + \frac{\partial}{\partial x}\int_0^h u \,\mathrm{d}z + \frac{\partial}{\partial y}\int_0^h v \,\mathrm{d}z = 0. \tag{2.22}$$

In common with other lubrication-type gravity current models, the shallow-ice approximation retains only leading-order terms, discarding contributions such as horizontal diffusion and velocity gradients; validity of this assumption, and its possible limitations at short wavelengths, are discussed in the following sections.

2.3. *Constitutive function*

Glen's flow law for non-isothermal ice is usually written in multiplicative form using an Arrhenius-type temperature dependence (Cuffey & Paterson 2010), giving

$$\hat{f}(\hat{T}, \hat{\tau}) = A \exp\left(-\frac{E}{R\hat{T}}\right)\hat{\tau}^n. \tag{2.23}$$

Here, E is the activation energy for creep, R is the universal gas constant, A is a constant rate factor and the exponent $n \approx 3$. In dimensionless form, this becomes

$$f(T, \tau) = \exp\left(\frac{T}{1 + \delta T}\right)\tau^n, \tag{2.24}$$

where $\delta = RT_a/E$. The Frank-Kamenetskii approximation takes $\delta \to 0$, leaving $f = \tau^n e^T$.

In the following sections, we will use the form (2.24) for f for illustrative numerical computations. We generally employ the full Arrhenius relation, but in some cases, when indicated, we also compare it with the Frank-Kamenetskii approximation. On the other hand, to maintain generality in the analytical results, we leave the form for this function open, and assume only that f is a non-negative function that is strictly increasing in both T and τ, implying

$$f(T, \tau) \geqslant 0, \quad f_T(T, \tau) > 0, \quad f_\tau(T, \tau) > 0, \quad \text{for all} \quad T, \tau \geqslant 0, \tag{2.25}$$

and $f \to 0$ as $\tau \to 0$, where subscripts T and τ once more denote differentiation. In practice, ensuring that $f_\tau > 0$ for all values of τ requires regularising the power law in (2.24), replacing τ^n for instance by $(\tau^2 + \tau_0^2)^{(n-1)/2}\tau$ with a small regularising parameter $\tau_0 \ll 1$. This becomes relevant in particular when dealing with the linearised version of the problem later, where we wish to avoid singular behaviour associated with vanishing shear stress at the ice surface.

2.4. *Parameters*

The independent dimensionless parameters in the model (2.14)–(2.22) are the thermal conductivity and thermal diffusivity ratios, K and κ, as well as the geothermal flux Γ,

https://doi.org/10.1017/jfm.2026.11984 Published online by Cambridge University Press

ρ	910 kg m^{-3}	—	—
c_p	2×10^3 J (kg K)$^{-1}$	—	—
A	3.62×10^{-13} 1 (s Pa^3)$^{-1}$	—	—
E/R	7.21×10^3 K	s	0–2
T_a	233 K	H	0.1–1
K_R	3.1 W (m K)$^{-1}$	K	1.42
K_I	2.18 W (m K)$^{-1}$	κ	1.33
κ_R	1.6×10^{-6} m^2 s^{-1}	n	3
κ_I	1.2×10^{-6} m^2 s^{-1}	Γ	5.6
G	0.06 W m^{-2}	δ	3.23×10^{-2}
$\mathcal{H}$	1.53 km	ε	9.32×10^{-3}
$\mathcal{U}$	2.64 m year^{-1}	—	—
$\mathcal{L}$	164 km	—	—

Table 1. Typical dimensional and dimensionless parameter values.

the activation energy parameter δ and power-law index n in the constitutive model (2.23), the slope parameter s and the mean depth of the ice H (cf. § 3). Glaciologically relevant values for these parameters are collated in table 1.

Recalling that $\mathcal{H}$ and $\mathcal{L}$ are chosen so that the Brinkmann and Péclet numbers are both unity, the dimensional parameter values in table 1 give $\mathcal{H} = 1.53$ km and $\mathcal{L} = 164$ km, as reported there. Although these should not be interpreted too literally as the depth and length of a particular glacier, they are of an order consistent with certain regions of the Greenland ice sheet.

In the remainder of the paper, we take s and H to be the main two control parameters of the ice-flow problem (because they are not material parameters but depend on the geometrical setting), treating all of $\{\kappa, K, \Gamma, \delta, n\}$ as secondary parameters that we do not vary. As we will show in the following sections, the appearance of different regimes in the flux–slope relation for the base flow depends on the values of some of these parameters and, in extreme cases, certain regimes may disappear altogether. However, the qualitative stability properties associated with each regime remain robust.

3. The base flow

The model admits a steady base-flow solution that is uniform in x, so that

$$u = U(z), \quad T = \Theta(z), \quad h = H, \quad v = w = 0. \tag{3.1}$$

The velocity and temperature profiles follow from

$$\left.\begin{aligned} \Theta_{zz} &= -F\bar{\tau} \\ U_z &= F \\ \bar{\tau} &= (H - z)s \end{aligned}\right\} \quad \text{in } 0 < z < H, \tag{3.2}$$

where $F = f(\bar{\tau}, \Theta)$, with boundary conditions

$$U(0) = \Theta(H) = 0 \quad \text{and} \quad \Theta_z(0) = -\Gamma. \tag{3.3}$$

The base solution has a net flux of

$$Q = \int_0^H U \,\mathrm{d}z \equiv \int_0^H \int_0^z f(\bar{\tau}(\zeta), \Theta(\zeta)) \,\mathrm{d}\zeta \,\mathrm{d}z \equiv \int_0^H (H - z)F \,\mathrm{d}z, \tag{3.4}$$

https://doi.org/10.1017/jfm.2026.11984 Published online by Cambridge University Press

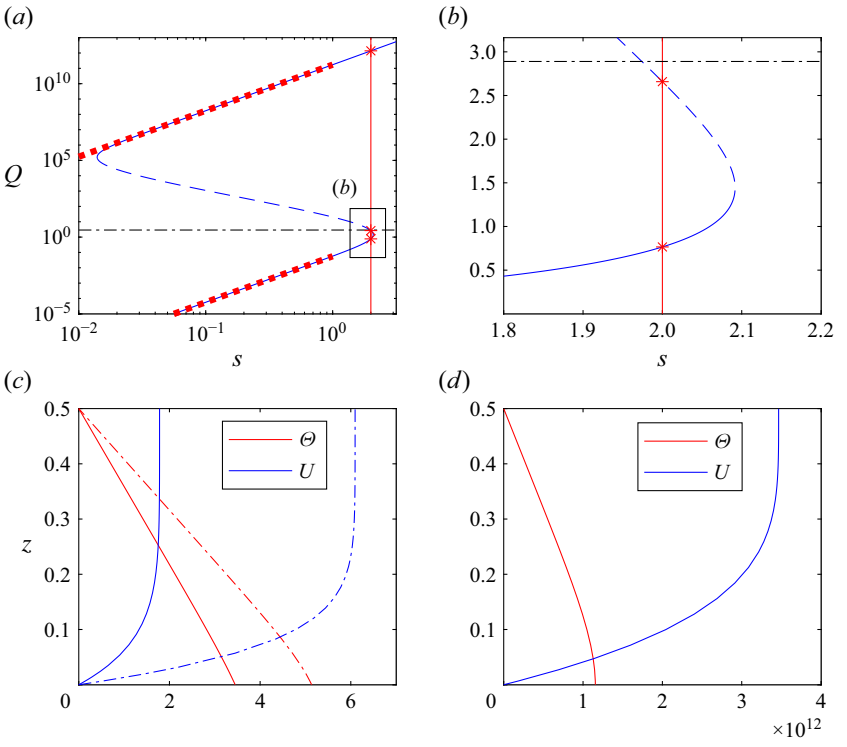


Figure 2. (*a*) Bifurcation diagram of base-flow solutions to (3.2)–(3.4) for $H = (1/2)$, with the remaining parameter settings listed in table 1. Above the dot-dashed line, the dimensional base temperature exceeds the melting point of ice if we use the typical parameter values in table 1. The thicker red dotted lines indicate the asymptotes for small and large Q. (*b*) Magnification of panel (*a*) around the first fold point. (*c*) Corresponding temperature and velocity profiles on branch 1 (solid lines) and branch 2 (dot-dashed lines) at $s = 2$ (indicated by the vertical solid lines and stars in panels (*a*) and (*b*)). (*d*) Same as panel (*c*), but for branch 3.

and bottom temperature of

$$\Theta(0) = \Gamma H - \int_0^H (H - z)\Theta_{zz}\,\mathrm{d}z = \Gamma H + s\int_0^H (H - z)^2 F\,\mathrm{d}z, \tag{3.5}$$

either of which can be used to characterise the base state as a function of slope s, given specific values of the other parameters $\{H, n, \Gamma, \delta\}$.

Earlier studies (Yuen & Schubert 1979; Hindmarsh 2004) also included a downward vertical velocity in the base flow, driven by a net accumulation of ice at the surface. Importantly, the resulting downward advection of heat adjusts the temperature distribution so that it becomes more like those observed for glaciers. Such base flows, however, cannot be uniform in x without some additional device that violates mass conservation. To follow their lead, we would have either to abandon the simplicity of the base-state problem above, or to add extra unphysical ingredients. We avoid these complications, accepting that the steady-state temperature distribution does not match that in typical ice sheets, where $T(z)$ is usually a convex function. In any event, Hindmarsh (2004) finds that vertical advection of the base state does not affect his numerical linear stability results qualitatively.

https://doi.org/10.1017/jfm.2026.11984 Published online by Cambridge University Press

3.1. *Multiple branches of the base-flow solution*

Sample solutions to the base-flow problem in (3.2)–(3.4) are presented in figure 2, which plots flux against slope for $H = (1/2)$. For $s \ll 1$ and using the Arrhenius relation ($\delta \neq 0$), the base-flow solution is

$$\Theta \sim \Gamma(H - z) \quad \text{and} \quad U \sim s^n H^{n+1} \int_{1-z/H}^{1} \zeta^n \exp\left(\frac{\Gamma H \zeta}{1 + \delta \Gamma H \zeta}\right) \mathrm{d}\zeta, \tag{3.6}$$

with a flux and basal temperature of

$$Q \sim s^n H^{n+2} \int_0^1 \zeta^{n+1} \exp\left(\frac{\Gamma H \zeta}{1 + \delta \Gamma H \zeta}\right) \mathrm{d}\zeta, \tag{3.7}$$

$$\Theta(0) \sim \Gamma H + s^{n+1} H^{n+3} \int_0^1 \zeta^{n+2} \exp\left(\frac{\Gamma H \zeta}{1 + \delta \Gamma H \zeta}\right) \mathrm{d}\zeta. \tag{3.8}$$

As shown in figure 2, the corresponding solution branch only extends to $s \approx 2.1$, at which point, the solution folds back on itself, generating a second branch of solutions with higher fluxes that decrease with increasing slope. At a second critical slope, the solution folds a second time, to generate a third branch with extremely high flux. On this branch, Θ becomes so large that it is acceptable to take the limit $\Theta \gg 1$ in (3.4)–(3.5), giving

$$Q \sim \frac{s^n H^{n+2} e^{1/\delta}}{n+2} \quad \text{and} \quad \Theta(0) \sim \Gamma H + \frac{s^{n+1} H^{n+3} e^{1/\delta}}{n+3}. \tag{3.9}$$

The potential for the existence of multiple branches in the flux–slope relation was shown in previous studies (Clarke *et al.* 1977; Yuen & Schubert 1979; Fowler 1980; Fowler & Larson 1980; Hindmarsh 2004). The dot-dashed lines in panels (*a*) and (*b*) indicate the melting-point threshold for the parameters in table 1. Above this line, the solution exceeds the melting point somewhere in the ice. In non-dimensional terms, this corresponds to $T \approx 5.31$ for the chosen parameters. Because the highest temperature occurs at the base, the threshold corresponds to a solution with basal temperature exactly at the melting point. Our model therefore breaks down above this threshold. For the parameter values considered here, branch 1 lies entirely below the threshold, and a portion of branch 2 does as well. Branch 3, however, lies entirely above it, so its analysis is purely mathematical rather than physically relevant.

Figure 2 also shows the temperature and velocity profiles of the three branches at $s = 2$. The unrealistic nature of branch 3 is evident in the extreme scale used in panel (*d*), whose magnitude is not physically plausible. The temperature field also illustrates the differing roles played by viscous dissipation, with the linear temperature profile in branch 1 (panel (*c*)) corresponding to negligible viscous heating and differing markedly from the concave profiles caused by significant dissipation on the other two branches. An asymptotic solution for the temperature profile for large basal temperatures such as those in branch 2 (panel (*c*)) can be found in Appendix C, showing that the concave part of the profile is in fact a boundary layer near the base of the ice, underlying a conduction-dominated region that extends across the remainder of the ice column.

Figure 3 shows how the basal temperature varies with slope, and compares the results using the Arrhenius relation with those for the Frank-Kamenetskii approximation. Notably, with the Frank-Kamenetskii approximation, the third branch vanishes, and the second branch continues monotonically to smaller slopes and higher basal temperatures.

https://doi.org/10.1017/jfm.2026.11984 Published online by Cambridge University Press

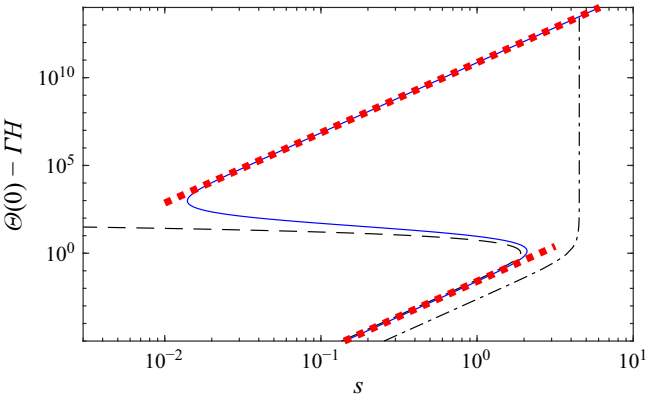


Figure 3. Relative base temperature, $\Theta(0) - \Gamma H$, plotted against the slope s for $H = (1/2)$ and the remaining parameter settings provided in table 1. The blue solid line represents the results obtained using the Arrhenius relation, while the black dashed line corresponds to those with the Frank-Kamenetskii approximation. The dot-dashed line shows Joseph's bound (Joseph 1966) and the thicker red dotted lines indicate the asymptotes for small and large $\Theta(0) - \Gamma H$.

The figure further includes the asymptotes at small values of $\Theta(0) - \Gamma H$, from (3.8), and large values of $\Theta(0) - \Gamma H$, from (3.9).

Analysis by Joseph (1966) can be used to place bounds on the regions where there are multiple solutions. We translate Joseph's analysis to the current problem in Appendix B, which shows that there can be no solutions to the right of the dot-dashed line added to figure 3. Note that a key element of Joseph's bound is that a certain function of the base temperature must remain positive (see Appendix B). This is violated for large $\Theta(0)$ with the Arrhenius law. The bound therefore disappears at sufficiently large base temperatures, allowing the upper branch to pass to the right of the dot-dashed line.

Figure 4(a) presents diagrams of Q against s for various values of the base height H. As the base height increases, the fold points move closer together until they collide at a codimension-2 cusp bifurcation, and vanish for larger base heights: beyond that threshold, the second branch disappears, and the first and third branches merge. Figure 4(c) is similar to figure 4(a), except that contours of H are shown in the (s, Q)-plane.

3.2. *Quasi-static flux*

As we have seen, the steady-state base solution predicts a flux through (3.4) that depends on the slope s and ice depth H: $Q = \mathcal{Q}(s, H)$. If this flux law were to extend to the full, time-dependent, two-dimensional problem with a mass source term a, then we could write

$$h_t + Q_x = a, \quad Q = \mathcal{Q}(S, h), \quad S = s - h_x. \tag{3.10}$$

The simplified system (3.10) permits a straightforward exploration of linear stability. For simplicity omit the source term a once more and perturb around a uniform steady state by setting $h = H + \eta(x, t)$, we obtain

$$\eta_t - \mathcal{Q}_s \eta_{xx} + \mathcal{Q}_H \eta_x = 0, \tag{3.11}$$

where

$$\mathcal{Q}_s = \frac{\partial \mathcal{Q}}{\partial s} \quad \text{and} \quad \mathcal{Q}_H = \frac{\partial \mathcal{Q}}{\partial H} \tag{3.12}$$

https://doi.org/10.1017/jfm.2026.11984 Published online by Cambridge University Press

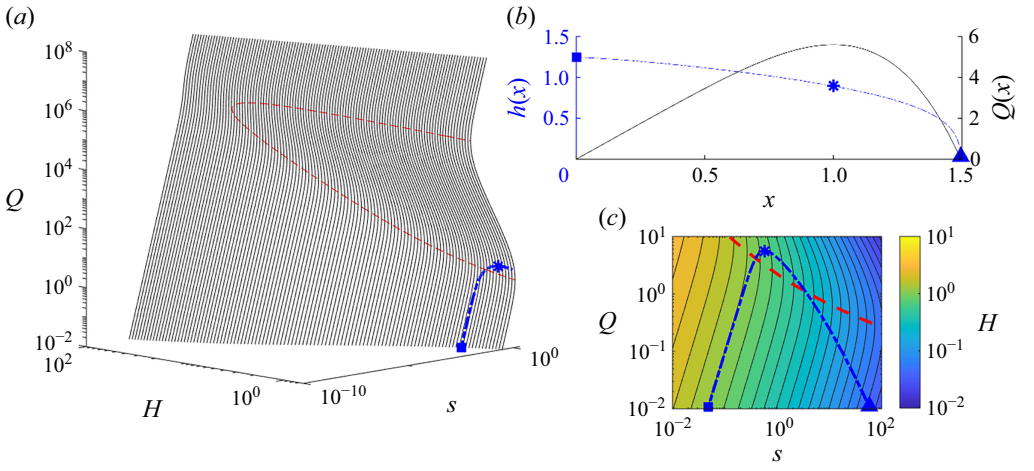


Figure 4. (*a*) Flux–slope relations for various values of the mean height H, with the remaining parameter values given in table 1. The dotted red line tracks the fold points. The blue dot-dashed line shows a trajectory on the (s, H, Q) surface corresponding to the non-uniform steady state computed from the two-dimensional problem with a mass source term (3.10) with $a(x) = 7(1 - x^4)$; details are given in the Appendix D. (*b*) Height (blue dot-dashed line) and flux (solid black line) as functions of x for this non-uniform steady state. (*c*) The trajectory associated with the non-uniform steady state, plotted over contours of H in the (s, Q)-plane. The blue square marks the ice divide, the blue star marks the point where the flux attains its maximum and the blue triangle marks the margin. These markers are included in every panel for reference.

denote the partial derivatives of the flux law, evaluated for the base flow. The sign of $\mathcal{Q}_s$ therefore dictates stability, implying that the first and third branches are expected to be stable. The intermediate second branch is expected to be unstable, and, indeed, the quasi-static approximation suggests an ill-posed backward-diffusion problem in which the growth rate diverges quadratically with wavenumber.

As shown in Appendix D, after including a prescribed mass source term $a(x)$, the system (3.10) also allows a non-uniform steady state with compact support to be computed on a flat bed (with $s = 0$), starting at a central ice divide ($x = 0$) and imposing vanishing ice thickness and flux at a free boundary representing the lateral edge or margin of the ice. A sample solution is shown in figures 4(*b*) and 4(*c*). At the ice divide, the flux vanishes by symmetry and surface slope vanishes, so the trajectory begins on branch 1. As x increases away from the divide, marked by the blue square, the flux initially increases as $a > 0$. The local surface slope $S = -h_x$ increases as well, so the trajectory moves upward along branch 1 until it crosses into branch 2. At the point where the flux attains its maximum, marked by the blue star, the trajectory turns and then proceeds toward smaller values of Q as the profile thins toward the margin, eventually returning to branch 1. Finally, at the margin, both H and Q vanish, and the trajectory terminates at the blue triangle. In this way, the trajectory provides a convenient geometric description of how the non-uniform steady state samples the local slab solutions and whether it remains on branch 1 or crosses the fold and enters branch 2. Clearly, steady-state solutions that cross onto branch 2 are possible (figure 4), making the properties of both branches 1 and 2 relevant to less idealised settings than the simple parallel-sided slab of (3.1)–(3.3).

The same stability problem (3.11) with the last term $\mathcal{Q}_H \eta_x$ omitted, arises in the short-wave perturbation limit of the non-trivial steady state constructed in Appendix D and displayed in figure 4. The stability properties remain the same, with the non-uniform

https://doi.org/10.1017/jfm.2026.11984 Published online by Cambridge University Press

steady-state solution being violently unstable to short-wavelength perturbations where the solution follows branch 2 of the flux–thickness–slope relationship. However, the underlying assumption of a quasi-static, low-Péclet-number temperature field ignores all effects of thermal relaxation, prompting us to turn to a more detailed analysis below that shows why the simple intuition we may gain from linearising a steady-state flux law as above is inaccurate.

4. Linear stability analysis

The linear stability of our model is analysed by expanding the variables as

$$[T, u, v, w] = [\Theta, U, 0, 0] + [\theta, u', v', w'](z)e^{ikx+ily+\sigma t} \quad \text{and} \quad h = H + \eta e^{ikx+ily+\sigma t}, \tag{4.1}$$

where (k, l) denotes the wavenumber, σ is the (complex) growth rate and $[\theta, u', v', w', \eta]$ are the infinitesimally small perturbation amplitudes. By substituting (4.1) into (2.14)–(2.22) and linearising in those amplitudes, we find, for $0 < z < H$

$$\sigma\theta + ikU\theta + w'\Theta_z = \theta_{zz} + F_T\bar{\tau}\theta + (F_\tau\bar{\tau} + F)\tau', \tag{4.2}$$

$$u'_z = F_\tau\tau' + F_T\theta, \tag{4.3}$$

$$v'_z = -ils^{-1}F\eta, \tag{4.4}$$

$$iku' + ilv' + w'_z = 0, \tag{4.5}$$

$$\tau' = -ik(H - z)\eta + s\eta, \tag{4.6}$$

where $F_\tau = f_\tau(\bar{\tau}, \Theta)$ and $F_T = f_T(\bar{\tau}, \Theta)$. The prescribed temperature condition at the surface of the ice becomes

$$\theta + \Theta_z\eta = 0 \quad \text{at } z = H. \tag{4.7}$$

The linear diffusion equation in the bedrock

$$\sigma\theta - \theta_{zz} = 0, \quad z < 0 \tag{4.8}$$

can be solved explicitly subject to $\theta_z \to 0$ as $z \to -\infty$. The boundary conditions at $z = 0$ then become

$$\theta_z = K\theta\sqrt{\sigma/\kappa} \quad \& \quad u' = v' = w' = 0, \tag{4.9}$$

where the branch taken for the square root $\sqrt{\sigma/\kappa}$ must have positive real part in order that perturbations decay for $z \to -\infty$. A convenient normalisation for the mode amplitudes is to take $\eta = 1$. Finally, the linearised depth-integrated mass conservation condition is

$$[\sigma + ikU(H)]\eta + ik\int_0^H u'\mathrm{d}z + il\int_0^H v'\mathrm{d}z = 0, \tag{4.10}$$

We break our analysis of this linear system down into three parts. First, we consider zero-wavenumber modes with spatial structure only in z ($k = l = 0$; § 4.1). We then allow for a wave-like structure in the streamwise direction ($l = 0$; § 4.2). Finally, we consider fully three-dimensional perturbations (§ 4.3). In each case, we complement a numerical exploration with a combination of variational techniques and asymptotics. For the numerical solution, the base flow is first found using the MATLAB boundary-value-problem solver BVP4C. The linearised problem is then solved by either turning the system

https://doi.org/10.1017/jfm.2026.11984 Published online by Cambridge University Press

into a large matrix eigenvalue problem after discretising spatial derivatives using centred finite differences (which generates many eigenvalues all at once), or again using BVP4C to track a particular eigenmode (requiring a guess for a specific eigensolution, provided either by the finite-difference scheme or a solution at different parameter settings). The former is limited by the finite resolution of the spatial grid, whereas the latter uses an adaptive grid that ensures the computation maintains a given error tolerance.

4.1. *Zero-wavenumber modes; $k = l = 0$*

The results from the quasi-static stability arguments of § 3.2 can be placed on a firmer basis by looking for solutions to the linear stability problem that depend only on z. That is, we set $k = l = 0$, reducing (4.2)–(4.10) to

$$\sigma\theta - \theta_{zz} - F_T\bar{\tau}\theta = 0, \quad 0 < z < H, \tag{4.11}$$

$$\theta_z - K\sqrt{\frac{\sigma}{\kappa}}\theta = 0, \quad \text{at} \quad z = 0, \tag{4.12}$$

$$\theta = 0, \quad \text{at} \quad z = H. \tag{4.13}$$

We will make repeated use later of the fact that a closely related problem is obtained by taking the equations (3.2)–(3.3) for the base flow and differentiating with respect to the parameter Q, in which case

$$-\Theta_{Qzz} - F_T\bar{\tau}\Theta_Q - s_Q(F_\tau\bar{\tau} + F)(H - z) = 0, \quad 0 < z < H, \tag{4.14}$$

$$\Theta_{Qz} = 0, \quad \text{at} \quad z = 0, \tag{4.15}$$

$$\Theta_Q = 0, \quad \text{at} \quad z = H, \tag{4.16}$$

where Θ_Q is the derivative of the base-flow solution with respect to flux Q. Moreover, substitution of (3.2) into (3.4) yields

$$Q = -\frac{1}{s}\int_0^H \Theta_{zz}\,\mathrm{d}z = -\frac{1}{s}\left(\Theta_z(H) + \Gamma\right). \tag{4.17}$$

Multiplying this expression by s and differentiating with respect to Q yields the additional condition

$$\Theta_{Qz} = -s_Q Q - s \quad \text{at} \quad z = H. \tag{4.18}$$

In the eigenvalue problem (4.11)–(4.13), the lower boundary condition ensures that this system is not of Sturm–Liouville type (Zettl 2005). However, the problem does take such a form if we consider the limit $K \to 0$, which is equivalent to imposing a constant heat flux at the base of the ice rather than solving a diffusion problem. We consider this special case first. In doing so, we also reconsider the parametric dependence of the base-flow solutions. In particular, because these solutions vary non-monotonically with s, we recast the base-state problem as one that is parametrised (implicitly) by Q, rather than s, which renders the parametric dependence single valued. The slope then becomes an output parameter of the base-flow problem, easily determined by reflecting plots like figure 2(*a*) about the line $Q = s$.

https://doi.org/10.1017/jfm.2026.11984 Published online by Cambridge University Press

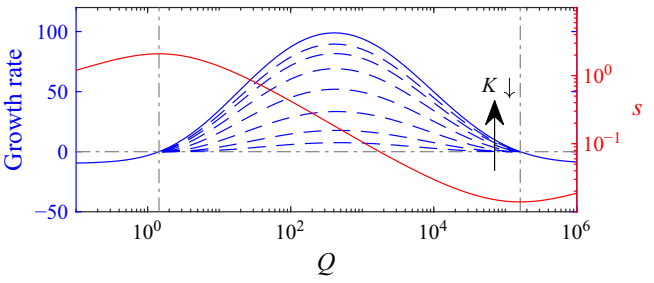


Figure 5. Growth rates of the largest eigenvalues as a function of Q. The solid line represents the growth rate from the Sturm–Liouville system ($k = l = K = 0$) described by (4.19)–(4.21), and the dashed lines correspond to the system described by (4.11)–(4.13) for $K = 6.4, 3.2, 1.6, 0.8, 0.4, 0.2, 0.1$. These computations were performed for $H = (1/2)$ and the remaining parameter settings listed in table 1. The vertical dot-dashed lines indicate the locations of the fold points, and the horizontal dot-dashed line indicates zero growth rate. Also shown is the slope of the base-flow solution.

4.1.1. *The Sturm–Liouville problem*

The $k = l = K = 0$ Sturm–Liouville problem is

$$\sigma\theta - \theta_{zz} - F_T\bar{\tau}\theta = 0, \quad 0 < z < H, \tag{4.19}$$

$$\theta_z = 0, \quad \text{at} \quad z = 0, \tag{4.20}$$

$$\theta = 0, \quad \text{at} \quad z = H. \tag{4.21}$$

Fold points occur when $s_Q = 0$. Comparing (4.19)–(4.21) with (4.14)–(4.16) at a fold point, we see that Θ_Q satisfies (4.19)–(4.21). Moreover, (4.18) shows that Θ_Q is not identically zero. It follows that there must be a zero eigenvalue at a fold point.

By multiplying (4.19) by Θ_Q, (4.14) by θ and integrating, we also find that

$$\sigma \int_0^H \theta\Theta_Q \mathrm{d}z = -s_Q \int_0^H \theta(F_\tau\bar{\tau} + F)(H - z)\mathrm{d}z. \tag{4.22}$$

Sturm–Liouville theory guarantees that eigenfunctions associated with the largest eigenvalue maintain a single sign. Our choice of constitutive function also implies that $F_\tau\bar{\tau} + F > 0$. Therefore, (4.22) confirms that a fold point must occur in the bifurcation diagram whenever the largest eigenvalue vanishes. For low values of the base flux ($Q \ll 1$), the third term in (4.19) can be omitted, resulting in a stable system with largest eigenvalue $\sigma = -(\pi/H)^2$. Consequently, the solution along the first branch must be stable for modes with $k = l = K = 0$.

A further derivative with respect to Q leads to the relation

$$\sigma_Q \int_0^H \Theta_Q\theta \mathrm{d}z = -s_{QQ} \int_0^H (F_\tau\bar{\tau} + F)(H - z)\theta \mathrm{d}z, \tag{4.23}$$

at fold points (since $s_Q = 0$ there). From (4.16) and (4.18), we conclude that, at the fold point, Θ_Q is positive in a neighbourhood of $z = H$. Moreover, at the fold point, Θ_Q is the eigenfunction associated with the largest eigenvalue and therefore does not change sign. As a result, $\Theta_Q \geqslant 0$ throughout the domain. Hence $\sigma_Q > 0$, implying that σ becomes positive along the second branch. This stability pattern is illustrated in figure 2, where the solid line represents stable solutions, while the dashed line indicates unstable solutions.

Figure 5 shows the growth rate of numerical solutions to (4.19)–(4.21) across the three branches, illustrating the transition of stability at each fold point. At the second fold point,

https://doi.org/10.1017/jfm.2026.11984 Published online by Cambridge University Press

we observe numerically that the leading eigenvalue again reverses sign, implying a return to stability along the third branch. This feature cannot be established directly from the preceding arguments because the second fold point could in principle correspond to the vanishing of either the largest or the second-largest eigenvalue.

Fowler & Larson (1980) previously analysed the Sturm–Liouville problem in (4.19)–(4.21). Without the benefit of numerical solutions to confirm their results, Fowler & Larson conclude that the base flow is always stable, even along the second branch. The root of their disagreement with our results lies in the properties of the eigenfunctions of the Sturm–Liouville problem (our θ, denoted by χ in their notation). Fowler & Larson (1980) claim that χ has self-similar structure under changes in a control parameter α (see their (29)); α is equivalent to s^{n+1} here, where s is slope and n the exponent in (2.24). The function χ, however, satisfies a particular version of our (4.19) ((24) in Fowler & Larson (1980)) in which the base profile $\Theta(z)$ (denoted by θ in their work) appears as a coefficient. The self-similar representation in their (29) is built on a rescaling of the vertical coordinate, $\xi \mapsto (\beta/\alpha)^{1/(n+3)}\xi$, and holds only if the base profile is invariant under this rescaling (only if $\theta(\xi)$ and $\theta((\alpha/\beta)^{1/(n+3)}\xi)$ coincide), which is not the case for the non-constant profiles at hand. This invalidates the remainder of their stability argument.

Indeed, our results above establish that the second branch is unstable, as already indicated by the numerical work in Hindmarsh (2004). Moreover, the linear stability analysis of the Couette, Poiseuille and Hagen–Poiseuille configurations, conducted by Joseph (1964), yields results consistent with ours. Lastly, our findings are in agreement with those of Joseph (1965*a*), who investigated the linear stability of temperature distributions in conducting solids with nonlinear heat generation. Although his model involves a heat generation term dependent only on temperature, his extension to non-planar geometries introduces a spatial dependence to the heating term, making it identical to our formulation.

4.1.2. *Finite bedrock diffusion*

We return now to the more general, non-self-adjoint problem (4.11)–(4.13), retaining diffusion in the bedrock. Multiply (4.11) by the complex conjugate of θ and integrate, to find on application of the boundary conditions that

$$\sigma \int_0^H |\theta|^2 \mathrm{d}z + \frac{K}{\sqrt{\kappa}}\sqrt{\sigma}|\theta(0)|^2 + \int_0^H |\theta_z|^2 \mathrm{d}z = \int_0^H F_T \bar{\tau}|\theta|^2 \mathrm{d}z. \tag{4.24}$$

Assuming σ has zero real part, so that $\sigma = i\sigma_i$ with $\sigma_i \in \mathbb{R}$, and taking the imaginary part of (4.24), we obtain

$$|\sigma_i| \int_0^H |\theta|^2 \mathrm{d}z + \frac{K}{\sqrt{2\kappa}}\sqrt{|\sigma_i|}|\theta(0)|^2 = 0, \tag{4.25}$$

thus $\sigma_i = 0$. In other words, if σ crosses the imaginary axis, it must do so through the origin. At a zero eigenvalue, the eigenvalue problems (4.11)–(4.13) and (4.19)–(4.21) are, however, identical, and we can therefore conclude that we can still only have $\sigma = 0$ in the non-self-adjoint problem (4.11)–(4.13) when $s_Q = 0$ as per (4.22). A change of stability at zero wavenumber can only happen at a fold point even when bedrock diffusion is retained in the problem.

Similarly to § 4.1.1, we can show that

$$\int_0^H [\lambda^2 \Theta_Q + s_Q(F_\tau \bar{\tau} + F)(H - z)]\theta \mathrm{d}z = -\frac{K}{\sqrt{\kappa}}\lambda\theta(0)\Theta_Q(0), \tag{4.26}$$

https://doi.org/10.1017/jfm.2026.11984 Published online by Cambridge University Press

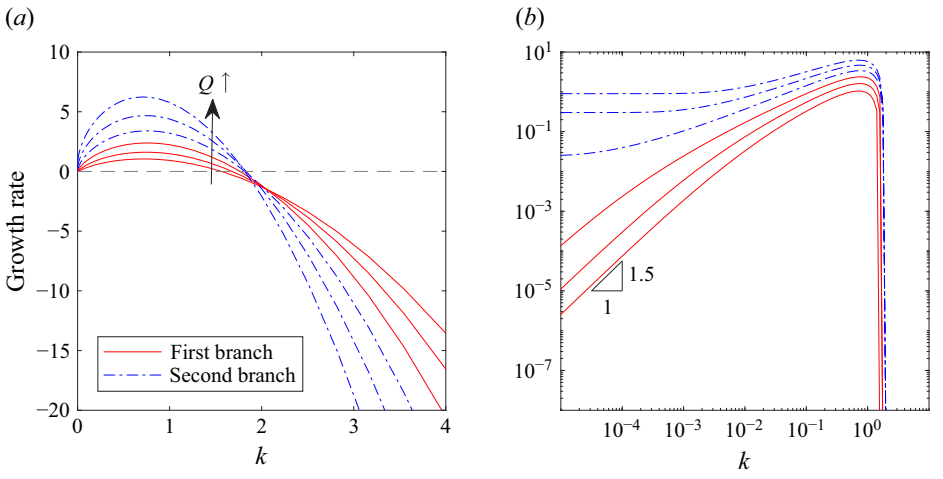


Figure 6. (*a*) Growth rate of the most unstable mode as a function of streamwise wavenumber k, for three values of the flux along the first ($Q = 10^{-0.1}$, 10^{0}, $10^{0.1}$; solid) and second ($Q = 10^{0.2}$, $10^{0.3}$, $10^{0.4}$; dot-dashed) branches, with $H = (1/2)$ and the parameters specified in table 1. The grey dashed line marks the zero axis. The growth rates are replotted using logarithmic axes in (*b*).

where $\lambda = \sqrt{\sigma}$ has positive real part. Differentiating with respect to Q at the fold ($\lambda = s_Q = 0$) results in

$$s_{QQ}\int_0^H (F_\tau \bar{\tau} + F)(H - z)\theta \mathrm{d}z = -\frac{K}{\sqrt{\kappa}}\theta(0)\Theta_Q(0)\lambda_Q. \tag{4.27}$$

At fold points, the eigenfunction θ corresponding to $\sigma = 0$ satisfies the same problem as Θ_Q, and hence $\theta \propto \Theta_Q > 0$. Thus, $\theta(0) \neq 0$ (since otherwise the problem is homogeneous with two homogeneous boundary conditions, admitting only the trivial solution $\theta \equiv 0$), λ_Q is real and

$$\mathrm{sgn}\left(\lambda_Q\right) = \mathrm{sgn}(-s_{QQ}). \tag{4.28}$$

Therefore, on passing the first fold point (where $-s_{QQ} > 0$), the real part of λ (and σ) becomes positive and remains so along the second branch. On the first branch below the fold, however, this argument implies that $\mathrm{Re}(\lambda)$ must be negative, which contradicts the requirement in the boundary conditions that λ has a positive real part. Therefore, the problem has no solutions that decay for $z \to -\infty$. The numerical solutions shown in figure 5 suggest that the unstable mode intersects and disappears into the continuous spectrum of non-spatially decaying modes at the fold points, consistent with the observation that we cannot find a solution for λ with positive real part.

4.2. *Modes without transverse structure* ($l = 0$)

For perturbations with streamwise spatial structure ($k > 0$), the range of unstable modes is much larger. In particular, when $K > 0$, all three branches become unstable over a finite range of wavenumbers k. The instability along the lowest and intermediate branches is illustrated in figures 6 and 7(*a*), where unstable modes extend from $k = 0$ up to an $O(1)$ critical wavenumber. Along the lower branch, $\sigma_r := \mathrm{Re}(\sigma) \propto k^{3/2}$ for $k \to 0$. In contrast, σ_r converges to the $O(1)$ growth rate of the zero-wavenumber problem considered in § 4.1.2 for the intermediate branch (figure 6*b*).

https://doi.org/10.1017/jfm.2026.11984 Published online by Cambridge University Press

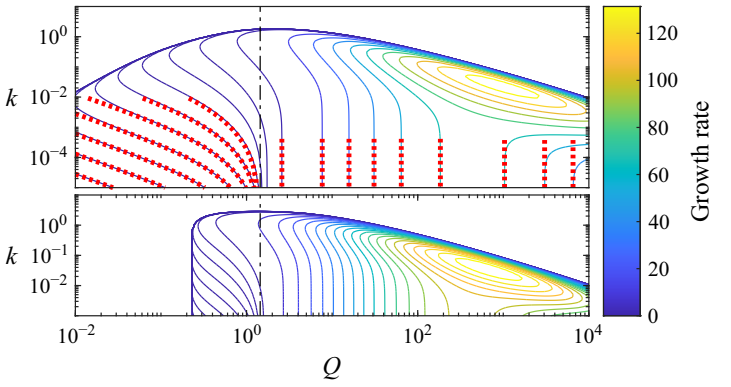


Figure 7. Contours of constant growth rate on the (Q, k)-plane, for (a) $K = 1.42$ and (b) $K = 0$, with $H = 1/2$, while the remaining parameters are specified in table 1. The (black) dot-dashed line indicates the first fold point. To the left of this line, the red dotted contours correspond to the long-wave asymptotic predictions, while to the right they represent the zero-wavenumber modes described in § 4.1.2. In each case, the growth rate along the dotted curves is matched to the corresponding contour value.

The stability properties of the lowest branch and the low-wavenumber behaviour are different when diffusion in the bedrock is ignored and a constant heat flux is imposed at the base of the ice ($K = 0$). In this case, the lowest branch is stable for sufficiently small flux (or slope), and a transition to instability arises at a critical value of Q that lies below the flux of the first fold point; see figure 7(b). Between that critical flux and the fold point, a window of unstable wavenumbers appears, with $\sigma_r \propto k^2$ for $k \to 0$.

The two variants of long-wave instability for $K > 0$ and $K = 0$ can be confirmed using asymptotic expansion for $k \ll 1$. We provide the analysis for the $K > 0$ case below.

4.2.1. *Long-wave instability of the first branch*

To explore linear stability in the long-wave limit, we use the asymptotic expansions

$$\sigma = k\sigma_0 + k^{3/2}\sigma_{1/2} + O(k^2), \quad \theta = \theta_0 + k^{1/2}\theta_{1/2} + O(k), \quad u' = u'_0 + k^{1/2}u'_{1/2} + O(k),$$
$$w' = kw'_0 + k^{3/2}w'_{1/2} + O(k^2), \quad Q' = Q'_0 + k^{1/2}Q'_{1/2} + O(k). \tag{4.29}$$

In view of our choice of normalisation of the eigenvalue problem ($\eta = 1$), the perturbation to the ice thickness η does not need to be expanded. At leading order we obtain

$$-\theta_{0,zz} = F_T\bar{\tau}\theta_0 + (F_\tau\bar{\tau} + F)\tau'_0, \tag{4.30}$$

$$u'_{0,z} = F_\tau\tau'_0 + F_T\theta_0, \tag{4.31}$$

$$\tau'_0 = \eta s, \tag{4.32}$$

for $0 < z < H$, with

$$\theta_{0,z} = u'_0 = 0, \quad \text{at} \quad z = 0, \tag{4.33}$$

$$\theta_0 + \Theta_z\eta = 0, \quad \text{at} \quad z = H, \tag{4.34}$$

and

$$\sigma_0\eta + iQ'_0 = 0, \quad Q'_0 = \int_0^H u'_0 \mathrm{d}z + U(H)\eta. \tag{4.35}$$

https://doi.org/10.1017/jfm.2026.11984 Published online by Cambridge University Press

By differentiating the base-flow equations with respect to the parameter H, while keeping all other parameters fixed, we derive the following relationship:

$$\frac{1}{\eta}\left[\theta_0,\, u_0',\, Q_0'\right] = \left[\Theta_H,\, U_H,\, Q_H\right]. \tag{4.36}$$

This result implies that the leading-order eigenvalue is $\sigma_0 = -i\,Q_H$, which is purely imaginary (Q_H is real). Hence, we must proceed to next order to assess the stability of the system.

At $O(k^{1/2})$, we find

$$-\theta_{1/2,zz} = F_T\,\bar{\tau}\,\theta_{1/2}, \quad u_{1/2,z}' = F_T\,\theta_{1/2}, \tag{4.37}$$

with

$$\theta_{1/2,z}(0) = K\sqrt{\sigma_0/\kappa}\;\theta_0(0), \quad u_{1/2}'(0) = 0, \tag{4.38}$$

$$\theta_{1/2}(H) = 0, \tag{4.39}$$

and

$$\sigma_{1/2}\eta + i\int_0^H u_{1/2}'\mathrm{d}z = 0. \tag{4.40}$$

Integrating by parts

$$\int_0^H u_{1/2}'\mathrm{d}z = \int_0^H\int_0^z F_T(\zeta)\theta_{1/2}(\zeta)\mathrm{d}\zeta\,\mathrm{d}z = \int_0^H (H-z)F_T(z)\theta_{1/2}(z)\mathrm{d}z. \tag{4.41}$$

Thus,

$$\sigma_{1/2} = -\frac{i}{s\eta}\int_0^H F_T\,\bar{\tau}\,\theta_{1/2}\mathrm{d}z, \tag{4.42}$$

since $\bar{\tau}/s = H - z$. The key is therefore to compute the integral on the right, or more specifically, to find the sign of its imaginary part. This requires us to determine the sign of the imaginary part of $\theta_{1/2}$, given that $F_T\,\bar{\tau} > 0$ and $\eta = 1$. It turns out that $\mathrm{Im}(\theta_{1/2}) > 0$ along the first branch, a result that is established in Appendix A. Numerically we find similar behaviour along the third branch.

Figure 8 compares the predictions of the long-wave analysis with numerical computations of σ_r. Also shown are the results from the zero-wavenumber analysis of § 4.1.2. One might assume that the instabilities of the first and second branches arise from different modes owing to the different behaviour in the limit $k \to 0$ on the two branches. Figure 8 shows that this is not the case, and that the most unstable modes are actually connected across the first fold point. This connection can be established, and the two disparate scalings with k reconciled, because the long-wave growth rate from (4.42) diverges as we approach the fold from the left, whereas the zero-wavenumber growth rate of the second branch vanishes on approaching from the right (see figure 8).

Note that the comparison between the asymptotic predictions and numerical results worsens for $k = 0.01$ and $Q = O(k)$ in figure 8, because, at these fluxes, there is a cross-over to a different asymptotic limit that applies for $Q \ll k \ll 1$. Also, the result in (4.42) highlights how the long-wave instability is insensitive to the detailed rheology of the ice. Indeed, the fluid could actually be Newtonian ($n = 1$) with a temperature-dependent

https://doi.org/10.1017/jfm.2026.11984 Published online by Cambridge University Press

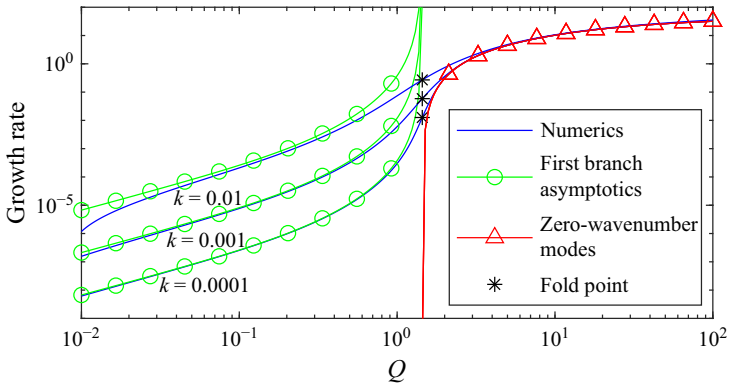


Figure 8. Numerically computed growth rates plotted against Q (solid blue lines) and compared with the predictions from long-wave asymptotics (green lines and circles) and the zero-wavenumber modes of § 4.1.2 (red lines and diamonds), for three values of k (as indicated), $H = (1/2)$ and the other parameter settings listed in table 1.

viscosity, and the flux–slope relation of the base states can be monotonically increasing and single valued (as is the case at small mean depths in figure 4), and the wave-like instability mechanism still persists.

4.2.2. *Physical mechanism*

The long-wave analysis above also helps to clarify the physical mechanism behind the instability: as illustrated in figure 9, flux increases with ice depth, causing regions near the crest of a wave to flow faster than regions near a trough. Consequently, areas where ice depth decreases downstream tend to accumulate material; areas of increasing ice depth tend to thin. The ice surface grows or shrinks to accommodate these variations, causing a wave to travel downstream. This wave is captured by the leading-order relations in the long-wave expansion in (4.30)–(4.35).

The presence of the wave affects the heat exchange between the ice and the bedrock, with excess heat generated within the ice underneath the wave crests, and diffusing into the underlying bedrock. This is the physical content of the $O(k^{1/2})$ corrections in (4.37)–(4.40). But the heat diffusion into the bed lags behind the wave crests (see figure 9), leading to additional heat retained in the ice on the upstream side of the wave, and cooler temperatures persisting below the downstream side of the wave. The combination reduces the viscosity where the layer is thinning, and enhances it where the layer thickens. This positive feedback, represented by (4.42) and facilitated by the diffusion of heat through the bedrock, causes the instability.

4.2.3. *Short-wave perturbations*

As observed in figures 6 and 7, modes with zero transverse wavenumber l in general become unstable only if the streamwise wavenumber lies within a finite range (whose size depends on model parameters), and large wavenumbers k are invariably stable. This contrasts markedly with the case of temperature-dependent sliding at the base of the ice (Mantelli & Schoof 2019), in which shallow-flow models remain unstable even at arbitrarily short streamwise wavelengths. To clarify the origin of this difference, we give an abbreviated analysis of the relevant asymptotic limit $k \gg 1$ here.

https://doi.org/10.1017/jfm.2026.11984 Published online by Cambridge University Press

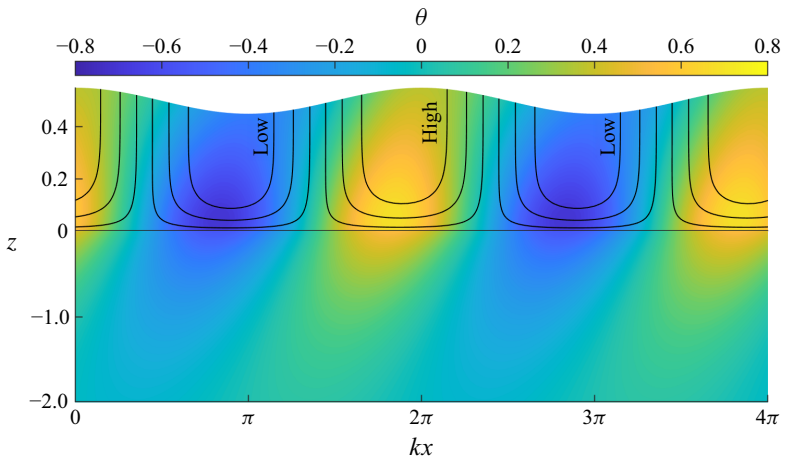


Figure 9. Colour map of the temperature perturbation θ on the (kx, z)-plane, for $H = (1/2)$, $k = 0.1$, $Q = 1$, $t = 0$ and the parameters in table 1. Black contours show the horizontal velocity perturbation u', and we have included an exaggerated surface perturbation to illustrate the relevant phase shifts.

The relevant leading-order behaviour is $\sigma = O(k^2)$, $\theta = O(1)$, $u' = O(k)$, $w' = O(k^2)$, $\tau' = O(k)$, $Q' = O(k)$ with $\eta = 1$, yielding, at leading order,

$$\sigma\eta + ikQ' = 0, \quad Q' = \int_0^H u' \mathrm{d}z, \quad u'_z = F_\tau \tau', \quad \tau' = -ik(H - z)\eta, \tag{4.43}$$

with $u' = 0$ at $z = 0$. This leads to

$$\sigma = -k^2 \int_0^H (H - z)^2 F_\tau(\bar{\tau}(z), \Theta(z))\mathrm{d}z < 0, \tag{4.44}$$

which decouples entirely from the thermal problem: temperature appears only parametrically through the base solution Θ in (4.44). The leading-order behaviour here is simply that of a diffusive highly viscous gravity current model, with a negative growth rate whose magnitude grows quadratically with wavenumber.

The fact that the flow problem can be decoupled from the thermal problem hinges on the leading-order versions of (4.2), (4.5) and (4.9) furnishing a suitable solution for w' and θ. The heat equation (4.2) demands that θ be determined by advection only at leading order, so that

$$\theta = -\frac{w'\Theta_z}{\sigma}, \tag{4.45}$$

while (4.9) demands at leading order that $\theta = -\Theta_z\eta$ at $z = H$ and $\theta = 0$ at $z = 0$. Ordinarily, we would expect boundary layers to appear at $z = 0$ and $z = H$, having reduced the second-order heat equation to an algebraic expression in (4.45). Indeed, thermal boundary layers are the cause of the short-wave instabilities in § 4 of Mantelli & Schoof (2019) for the case of temperature-dependent basal sliding. Here, in the absence of sliding and of heat dissipation at the bed itself, the purely advective solution (4.45) does not run into such problems: the vertical velocity, given by

$$w'(z) = -ik \int_0^z u'(z')\mathrm{d}z', \tag{4.46}$$

https://doi.org/10.1017/jfm.2026.11984 Published online by Cambridge University Press

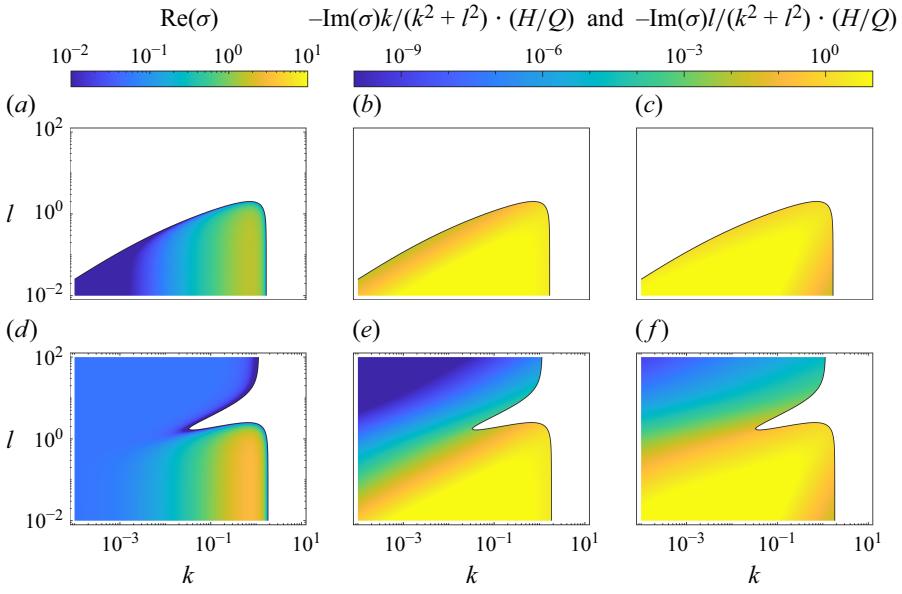


Figure 10. Colour maps over the (k, l)-plane for (*a*,*d*) growth rate $\mathrm{Re}(\sigma)$, and (*b*,*e*) streamwise and (*c*,*f*) cross-stream phase speed, of the most unstable mode at (*a*,*b*,*c*) $Q = 1$ and (*d*,*e*,*f*) $Q = 2$; $H = (1/2)$ and the other parameter settings listed in table 1. The phase speeds, $-\mathrm{Im}(\sigma)(k, l)/(k^2 + l^2)$, are scaled by the mean speed of the base flow, Q/H. Note that in (*d*) the growth rate plateaus at a finite value (≈ 0.1, dark blue) as l increases. Note also the logarithmic colour scale; regions in white correspond to negative growth rates.

satisfies $w' = 0$ at $z = 0$, and hence the boundary condition $\theta = 0$ holds there. Moreover, at $z = H$, $w' = -ikQ' = \sigma\eta$ and the surface boundary condition $\theta - w'\Theta_z/\sigma = -\Theta_z\eta$ also holds automatically.

4.3. *Three-dimensional perturbations* $(k, l > 0)$

The diffusive behaviour of the problem in one horizontal dimension deduced in § 4.2.3 is in fact deceptive, as we see when considering fully three-dimensional perturbations. Sample growth rates for such perturbations are plotted in the (k, l)-plane in figures 10(*a*) and 10(*d*). The remaining panels present the corresponding results for the two components of the phase velocity, $-\mathrm{Im}(\sigma)\boldsymbol{k}/|\boldsymbol{k}|^2$ (where $\boldsymbol{k} = (k, l)$ is the usual wave vector), each scaled by the mean speed of the base flow, Q/H. Panels (*a*,*b*,*c*) shows the results for an example along the first branch; panels (*d*,*e*,*f*) illustrates a case along the second branch. For the first branch, we recover the window of unstable wavenumbers in k for low l; increasing the transverse wavenumber l eventually suppresses the instability, rendering stable all the modes with higher l. By contrast, although an increase in transverse wavenumber initially still suppresses the unstable window in k along the second branch, a different regime of instability appears at higher l. This suppression can be traced to the transverse flux in the depth-integrated mass conservation (4.10): a transverse thickness perturbation drives a transverse flux that acts diffusively on η, contributing a stabilising term $\propto -l^2$ to the growth rate, even though no explicit transverse diffusion appears in the model. Stability boundaries, illustrating the two regimes for several values of flux Q, are shown in figure 11.

https://doi.org/10.1017/jfm.2026.11984 Published online by Cambridge University Press

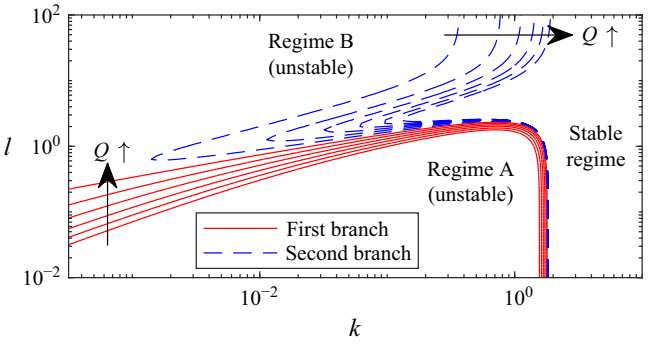


Figure 11. Stability boundaries on the (k, l)-plane for different values of the base flux along the first ($Q = 10^{-0.1}$, $10^{-0.05}$, 10^{0}, $10^{0.05}$, $10^{0.1}$, $10^{0.15}$; red, solid) and second branches ($Q = 10^{0.2}$, $10^{0.25}$, $10^{0.3}$, $10^{0.35}$, $10^{0.4}$, $10^{0.45}$; blue, dashed) for $H = (1/2)$ and the remaining parameter settings listed in table 1.

The two different unstable regimes were identified previously by Hindmarsh (2004). As in Hindmarsh's work, we will continue to refer to them as regimes A and B. Regime A appears for all branches and is characterised by small to order-one values of both wavenumbers. Regime B arises only for the intermediate branch, and is characterised by a flat plateau in growth rate at higher transverse wavenumbers and small to order-one values of k. As illustrated in figure 10, the unstable modes of regime A have significant phase speeds (up to six times the average base-flow speed). By contrast the phase speeds of the unstable modes in regime B are much lower, and approach zero for large enough transverse wavenumber l.

Figure 10 also shows that regime A typically features higher growth rates than regime B. This property is illustrated further in in figure 12(a), which plots the ratio of the maximum growth rate in regime B to that in regime A as a density over the (H, Q)-plane. The parameter space shown in this figure corresponds to base flows along the second branch for which the base temperature lies below the melting point of ice. Figure 12(b) also plots the streamwise wavenumber k at which maximum growth occurs (in regime A). The maximum growth rate typically occurs for $l = 0$ and $k = \mathrm{ord}(1)$, except at the smallest mean depths, where k for the most unstable mode becomes larger.

Figure 13 shows how the instability varies across the (H, Q)-plane along the first and second branches, with the red dashed line marking the fold points. Figure 13(a) displays the maximum growth rate over all wavenumbers. The fold-point curve is clearly associated with the contours of largest growth, indicating that the strength of the instability is strongly linked to the branch structure. The instability is weaker on the first branch, but strengthens as one approaches the fold point and crosses onto the second branch. There, the maximum growth rate continues to increase, reaches a peak and then decreases. On the other hand, the maximum growth rate decreases monotonically as H increases. In all cases, this maximum occurs at $l = 0$, and figure 13(b) shows the corresponding phase speed scaled by the mean speed of the base flow, $-H\mathrm{Im}(\sigma_{max})/(kQ)$. Over the parameter range explored, this scaled phase speed varies only moderately, taking values between approximately 6 and 10, and increasing as Q decreases and H increases. The more significant variation in scaled phase speed occurs between regimes A and B; however, since the maximum overall growth rate always belongs to regime A, this difference remains moderate in the present figure.

https://doi.org/10.1017/jfm.2026.11984 Published online by Cambridge University Press

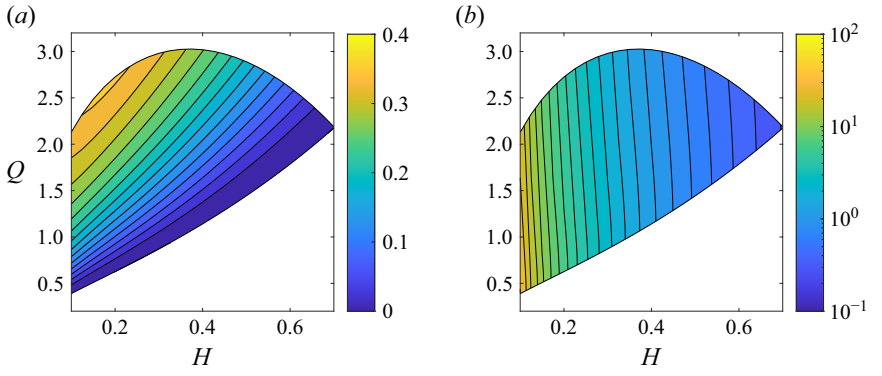


Figure 12. Contours on the $(H,\ Q)$-plane of (*a*) the ratio of maximum growth rate in regime B to that in regime A, and (*b*) the streamwise wavenumber k maximising growth. The white region below the contours corresponds to the first branch (where there is no regime B); that above locates where base temperatures surpass the melting point.

In view of the resolution-dependent thermal spokes in the numerical solutions of Payne & Baldwin (2000), the most pertinent feature of the three-dimensional dispersion relation is, however, not the fastest growth rate, but the fact that growth rates remain positive and bounded away from zero for arbitrarily large l in regime B. This motivates us to delve further into the relevant short-wave asymptotics for transverse perturbations.

For $l \gg 1$ and $k = O(1)$ in regime B, numerical experiments suggest that the solution to (4.2)–(4.10) behaves as $\sigma = O(1)$, $\theta = O(1)$, $u' = O(1)$, $v' = O(l^{-1})$, $w = O(1)$, $Q' = O(1)$, $\tau' = O(l^{-2})$ with $\eta = O(l^{-2})$, resulting in a leading-order problem of the form

$$\sigma\theta + ikU\theta + w'\Theta_z = \theta_{zz} + F_T\bar{\tau}\theta, \tag{4.47}$$

$$u'_z = F_T\theta, \tag{4.48}$$

$$v'_z = -ils^{-1}F\eta, \tag{4.49}$$

$$iku' + ilv' + w'_z = 0, \tag{4.50}$$

$$\tau' = -ik(H-z)\eta + \eta s, \tag{4.51}$$

subject to $u' = v' = w' = 0$ at $z = 0$, as well as

$$\theta_z = K\theta\sqrt{\sigma/\kappa} \quad \text{at } z = 0, \quad \theta = 0 \quad \text{at } z = H, \tag{4.52}$$

while the mass conservation (4.10) becomes

$$ik\int_0^H u'\mathrm{d}z + il\int_0^H v'\mathrm{d}z = 0. \tag{4.53}$$

From (4.53) and (4.50), we can then conclude that

$$\eta = -\frac{sik}{l^2}\frac{\int_0^H (H-z)F_T(z)\theta(z)\mathrm{d}z}{\int_0^H (H-z)F(z)\mathrm{d}z}, \tag{4.54}$$

https://doi.org/10.1017/jfm.2026.11984 Published online by Cambridge University Press

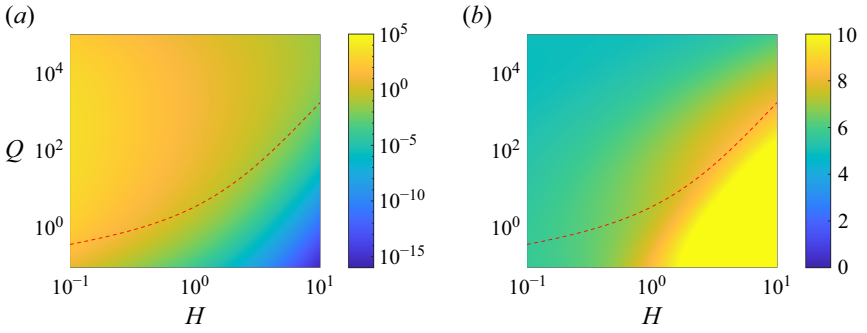


Figure 13. Colour plots on the (H, Q)-plane of (a) the maximum growth rate over all wavenumbers, and (b) the corresponding streamwise phase speed scaled by the mean speed of the base flow. The red dashed line marks the first fold point; the region above it corresponds to branch 2, and the region below it to branch 1.

$$w' = -ik\int_0^z (z-z')F_T(z')\theta(z')\mathrm{d}z' + ik\frac{\int_0^H (H-z')F_T(z')\theta(z)\mathrm{d}z'}{\int_0^H (H-z')F(z')\mathrm{d}z'}\int_0^z (z-z')F(z')\mathrm{d}z'. \tag{4.55}$$

As can be seen, substituting (4.55) into (4.47) together with the boundary conditions (4.52), yields an integro-differential eigenvalue problem for θ and σ contains no dependence on l.

This problem rationalises why the eigenvalue σ becomes independent of l for $l \gg 1$ in figure 10(d), emphasising how the growth rate does not vanish at large wavenumbers. Moreover, in the simultaneous limit of small k, ikU and w' both vanish. In that case, the integro-differential eigenvalue problem above becomes identical to the simpler one in (4.11)–(4.13). In other words, the behaviour of regime B for short transverse wavelengths and long streamwise wavelengths ($l \gg 1$ and $k \ll 1$) is actually given by the zero-wavenumber ($k = l = 0$) problem of § 4.1.2. In fact, setting $k = 0$ and looking for modes with $\eta = 0$ in the full stability problem (4.2)–(4.10) again leads to the same problem (4.11)–(4.13) regardless of the value of l.

As shown in § 4.1.2, (4.11)–(4.13) admit an eigenvalue with positive real part on the second, intermediate branch but not the first and third branches when $k = l = 0$. In fact, there is no solution to (4.11)–(4.13) on the first and third branches. As confirmed by our numerical results as well as those in Hindmarsh (2004), these results now carry over to the limit $k \ll 1$ regardless of the value of l: regime B exists only on the second, intermediate branch, and corresponds to instability without any short-wavelength stabilisation in the transverse direction.

4.4. *Nonlinear evolution of transverse perturbations*

Physically, the $k = \eta = 0$ case corresponds to adjacent columns of ice (at different values of y) decoupling from each other. We can exploit that insight to go beyond the linearised model we have looked at so far, and consider a simple version of the nonlinear problem (2.14)–(2.22) in order to better understand the implications of the missing short-wavelength cutoff. Suppose we restrict ourselves to initial conditions in which ice thickness h is a constant and temperature is independent of the streamwise coordinate x, as represented by the $k = 0$ mode with $\eta = 0$ in the linearised model. Then, h is constant

https://doi.org/10.1017/jfm.2026.11984 Published online by Cambridge University Press

in time and space, with $T = T(y, z, t)$ and $v = w = 0$ at all times. Consequently, T satisfies

$$\begin{aligned} T_t - T_{zz} &= \bar{\tau} f(\bar{\tau}, T) \quad \text{for } 0 < z < h, \\ T_t - \kappa T_{zz} &= 0 \qquad\qquad\quad \text{for } z < 0, \end{aligned} \tag{4.56}$$

subject to $T = 0$ at $z = h$, $T_z \to -\Gamma/K$ as $z \to -\infty$, and continuity of temperature and flux at $z = 0$. Here $\bar{\tau}(z) = s(h - z)$ is the base solution for shear stress, which also remains constant in time.

The transverse coordinate y does not appear explicitly anywhere in this geometrically reduced problem, either by way of parameters or through derivatives, and T still evolves independently in each ice column. As a result, if the initial temperature varies with y, then at each transverse location the solution may relax toward either the lower or the upper branch in figure 2(*a*), leading to a piecewise continuous steady state given continuous initial data. The solution presumably still depends continuously on the initial data for any finite time t, and the problem does not appear to be ill posed as suggested by Hindmarsh (2004, 2011).

The discontinuities involved in a piecewise continuous solution can be regularised by restoring the transverse diffusion term T_{yy}. The resulting system

$$\begin{aligned} T_t - \varepsilon^2 T_{yy} &= T_{zz} + \bar{\tau} f(\bar{\tau}, T) \quad \text{for } 0 < z < h, \\ T_t - \kappa\varepsilon^2 T_{yy} &= \kappa T_{zz} \qquad\qquad\quad \text{for } z < 0, \end{aligned} \tag{4.57}$$

subject to the same boundary and interface conditions, is analogous to an Allen–Cahn-type system (Bartels 2015). Here, the local dynamics is governed not by a scalar reaction term, but by a differential operator in z. Nevertheless, the analogy is appropriate because the local problem admits two stable steady states in the form of distinct vertical temperature profiles, corresponding precisely to the lower and upper branch base states. One may therefore expect the solution to separate into transverse regions that relax toward different branches, with sharp jumps replaced by narrow transition layers between them. In this sense, the dynamics is analogous to phase separation.

In addition to transverse diffusion of heat, lateral discontinuities in T and therefore in u will also be regularised by transverse shear stresses τ_{12}, which have also been omitted in our leading-order model, but affect the calculation of $\bar{\tau}(y, z) = \tau_{12}$ in (4.57) when retained.

5. Discussion

In this paper, we have explored the flow of a shallow layer of ice over inclined bedrock, subject to a constant geothermal heat flux. For certain parameter ranges, this problem admits multiple steady-state solutions for flows of uniform thickness, and the flux traces out an S-shaped curve when plotted as a function of bedrock slope (Clarke *et al.* 1977; Yuen & Schubert 1979; Fowler 1980; Fowler & Larson 1980; Hindmarsh 2004). Assuming this flux–slope relation governs the evolution of perturbations in the ice surface would suggest that the upper and lower branches are stable, while the intermediate branch is unstable. This is indeed correct if perturbations are independent of the horizontal coordinates (§ 4.1), in which case the instability of the intermediate branch takes the form of a thermal runaway arising from the coupling between viscous heating and temperature-dependent rheology (Robin 1955; Fowler 1997), closely related to Joseph's instability of frictionally heated and variable-viscosity flows (Joseph 1964, 1965*b*).

https://doi.org/10.1017/jfm.2026.11984 Published online by Cambridge University Press

This thermal runaway is damped at short wavelengths, and in the high-wavenumber limit the problem reduces to a stable forward-diffusion problem (§ 4.2.3). This contrasts with 'shallow-ice'-type lubrication models with temperature-dependent sliding (Mantelli *et al.* 2019; Mantelli & Schoof 2019), which remain unstable at arbitrarily short wavelengths. The discrepancy appears to be tied to the thermal boundary layers that arise in models with sliding, pointing to fundamental differences between thermally activated sliding and creeping motion concentrated near the glacier base.

Perhaps surprisingly, a linear stability analysis with streamwise perturbations also reveals that the lower and upper branches are no longer stable, at least when heat is allowed to diffuse into the underlying bed (§ 4.2). The long-wave analysis ($k \ll 1$) establishes this analytically (§ 4.2.1) and clarifies the physical processes causing the instability, which originates from phase lags in ice temperature induced by thermal diffusion through the bed (§ 4.2.2). This instability does not depend on special details of the rheology. It is enough that viscosity decreases with temperature; the fluid could otherwise be Newtonian. Nor does the instability require multiple base states: it can arise even when the mean flux depends monotonically on slope. The essential ingredient is diffusion through the bed.

The latter point is underscored by the fact that parts of the lowest branch can be stabilised by fixing the heat flux at the base of the ice layer (figure 7*b*), thereby removing diffusion through the bed. Even then, however, the lowest branch still becomes unstable at a critical flux below the fold point where the lowest and intermediate branches meet. This residual instability is weaker and appears to result from additional phase lags caused by thermal diffusion across the ice thickness together with differential advection by the vertical shear flow.

For fully three-dimensional perturbations, transverse structure suppresses instability along the lowest branch. Along the intermediate branch, however, it does not suppress the thermal runaway: instability persists for all transverse wavenumbers, with a growth rate bounded away from zero (§ 4.3). In this setting, the two instability regimes identified by Hindmarsh (2004) reappear. Regime A, which occurs on all branches, is still suppressed by transverse structure. Regime B, in contrast, is specific to the intermediate branch and persists even as the transverse wavenumber increases.

Although regime A is generally the stronger instability in terms of growth rate, with the largest growth rate occurring for modes with no transverse structure ($l = 0$), the associated waves also have significant downstream phase speeds, suggesting that such disturbances may be advected rapidly out of a finite domain. As shown in figure 4, finite steady states that are non-uniform in x can contain regions that cross into branch 2 and are therefore susceptible to this instability when the Péclet number is zero. Whether this remains true at non-zero Péclet number is not clear. It is therefore possible that the instability identified here is relevant to the onset of surging. However, glacier surging, in which ice motion alternates between brief episodes of rapid advance and longer intervals of slower retreat (Fowler & Larson 1978), is generally associated more strongly with variations in basal sliding (Kamb *et al.* 1985; Murray *et al.* 2003) than with internal thermo-viscous instability alone (Clarke 1976; Payne 1995; Fowler *et al.* 2001). For this reason, we do not suggest that the present mechanism explains surging by itself, but it may form part of a thermally regulated surge mechanism by causing instability in a steady state, with the instability evolving into oscillatory dynamics that eventually causes the ice–bed contact to reach the melting point, precipitating a fully fledged surge.

Regime B is usually weaker, but its phase speeds are much lower. Combined with its preference for lower streamwise wavenumbers and its persistence across all transverse wavenumbers, this suggests a more fingering-like appearance. It may therefore be relevant to the initiation of localised, finger-like ice streams (Hindmarsh 2004). However, given

https://doi.org/10.1017/jfm.2026.11984 Published online by Cambridge University Press

that our model is highly idealised and assumes no slip at the bed, it misses basal processes that are important in real ice streams. We therefore view these results as illustrative (and more relevant to the initiation of ice streams than to their fully developed state) rather than as a direct model of real glacier behaviour.

The lack of transverse wavelength selection, however, implies eventual loss of regularity and an attendant sensitivity to initial conditions and numerical resolution. Similar concerns have been raised previously for the shallow-ice approximation (Payne & Baldwin 2000; Saito *et al.* 2006; Hindmarsh 2009). A related thermo-viscous fingering instability has also been studied for magma flow through a narrow gap (Helfrich 1995), where linear theory predicts both a maximum growth rate and a short-wave cutoff. Unlike the standard shallow-ice approximation, Helfrich's model retains transverse heat diffusion. The need for a short-wavelength cutoff in a model for thermo-viscous instabilities while retaining as many of the simplifying features of a 'shallow ice' points to an obvious avenue for future research. The majority of models used in practice in glaciology use a higher-order thin-film approach to retain additional stress components (e.g. Brinkerhoff & Johnson 2015), but such models remain valid only in the limit of a small aspect ratio (Schoof & Hindmarsh 2010), and it remains unclear whether the use of such models can be justified when describing thermo-viscous instabilities. We will address in a separate paper the necessary modifications to the standard shallow-ice model required to lead to a short-wavelength cutoff while remaining faithful in an asymptotic sense to the underlying Stokes flow problem.

Funding. This research has been supported by the Natural Sciences and Engineering Research Council of Canada (grant nos. RGPIN-2022-03705 and RGPIN-2024-06422).

Declaration of interests. The authors report no conflict of interests.

Appendix A. $\mathrm{Im}(\theta_{1/2}(z)/\eta)$

In this appendix, we restrict ourselves to a branch of the steady-state solution on which the associated Sturm–Liouville problem (4.19) has only non-positive eigenvalues.

First, we show that $\Theta_H = \theta_0(0)/\eta > 0$ throughout the interval $[0, H)$. Doing so later allows us to find the sign of the real and imaginary parts of $\theta_{1/2}/\eta$, with $\theta_{1/2}$ depending on θ_0 through (4.38).

Consider the boundary value problem

$$-\Phi_{zz} - F_T\bar{\tau}\Phi = f, \quad \Phi_z(0) = 0, \quad \Phi(H) = 0, \tag{A1}$$

where f is an arbitrary function. The method of variation of parameters provides a Green's function for the problem. Specifically,

$$\Phi(z) = \int_0^H G(z, z')f(z')\mathrm{d}z', \tag{A2}$$

where

$$G\left(z, z'\right) = \begin{cases} \phi_1(z)\phi_2\left(z'\right)/(-W) & \text{if } z' < z, \\ \phi_1\left(z'\right)\phi_2(z)/(-W) & \text{if } z' \geqslant z, \end{cases} \tag{A3}$$

with $W = \phi_{1,z}\phi_2 - \phi_{2,z}\phi_1$ the Wronskian, and ϕ_1 and ϕ_2 satisfying

$$-\phi_{1,zz} - F_T\bar{\tau}\phi_1 = 0, \quad \phi_{1,z}(0) = 1, \quad \phi_1(H) = 0, \tag{A4}$$

https://doi.org/10.1017/jfm.2026.11984 Published online by Cambridge University Press

and

$$-\phi_{2,zz} - F_T\bar{\tau}\phi_2 = 0, \quad \phi_{2,z}(0) = 0, \quad \phi_2(H) = 1, \tag{A5}$$

respectively.

By linearity and from (4.30), we may now write

$$\Theta_H(z) = \frac{\theta_0(z)}{\eta} = \int_0^H G\left(z, z'\right)\left[F_\tau\left(z'\right)\bar{\tau}\left(z'\right) + F\left(z'\right)\right] s\,\mathrm{d}z' - \Theta_z(H)\phi_2(z). \tag{A6}$$

In order to show that $\theta_0(z)/\eta > 0$ for $0 \leqslant z < H$, it therefore suffices to show that $\phi_1 < 0$ and $\phi_2 > 0$ throughout the interval $[0,\, H)$. It then follows that $G > 0$, since the Wronskian is $W = \phi_2(0) > 0$ at $z = 0$, and W remains constant across the domain. With $G > 0$ and $\phi_2 > 0$, both terms on the right-hand side are positive since $F_\tau\bar{\tau} + F > 0$ and $\Theta_z(H) < 0$.

In order to show the required properties of ϕ_1 and ϕ_2, we can use the following modification of the classical Sturm–Picone comparison theorem.

Modification of the Sturm–Picone theorem: let θ_α and θ_β satisfy

$$\left.\begin{aligned}(p_\alpha\theta_{\alpha z})_z + q_\alpha\theta_\alpha = 0,\\ (p_\beta\theta_{\beta_z})_z + q_\beta\theta_\beta = 0\end{aligned}\right\} \tag{A7}$$

on the interval $I = [z_0, z_1]$ or $[z_1, z_0]$, subject to the conditions

$$a\,p_\alpha\theta_{\alpha z} + b\theta_\alpha = a\,p_\beta\theta_{\beta_z} + b\theta_\beta = 0 \quad \text{at } z = z_0, \tag{A8}$$

where p_α and p_β are strictly positive and $p_{\alpha z}$, p_{β_z}, q_α, q_β are continuous. Suppose

$$p_\beta \leqslant p_\alpha \quad \text{and} \quad q_\beta \geqslant q_\alpha. \tag{A9}$$

If $\theta_\alpha(z_1) = 0$, then there must be some point $\hat{z} \in I$ such that $\theta_\beta(\hat{z}) = 0$. Consequently, if $\theta_\beta(z)$ does not vanish in the interior of I, neither does $\theta_\alpha(z)$. Moreover, if θ_β does not vanish and $q > 0$ in the interior of I, but $\theta_{\beta_z}(z_s) = 0$ for some $z_s \in I$, then $\theta_{\alpha z}(z_s)$ either has the same sign as $\theta_{\alpha z}(z_0)$, or $\theta_{\alpha z}(z_s) = 0$.

Proof. This follows from the Prüfer substitution

$$\theta_\alpha = r_\alpha\sin(\alpha), \quad p_\alpha\theta_{\alpha z} = r_\alpha\cos(\alpha), \tag{A10}$$

which leads to

$$r_{\alpha z} = \left(\frac{1}{p_\alpha} - q_\alpha\right) r_\alpha\sin(\alpha)\cos(\alpha), \quad \alpha_z = \frac{1}{p_\alpha}\cos^2(\alpha) + q_\alpha\sin^2(\alpha) \tag{A11}$$

with analogous relations for θ_β and θ_{β_z} in terms of the transformed variables r_β and β. In particular

$$\beta_z = \frac{1}{p_\beta}\cos^2(\beta) + q_\beta\sin^2(\beta). \tag{A12}$$

In other words, we have $\alpha_z = \psi_\alpha(\alpha, z)$ and $\beta_z = \psi_\beta(\beta, z)$ where ψ_α and ψ_β are continuous, uniformly Lipschitz continuous in their first argument and satisfy $\psi_\beta(s, z) \geqslant \psi_\alpha(s, z)$ on account of (A9). Moreover, without loss of generality (replacing α with $-\alpha$ or β with $-\beta$ throughout as necessary), we can put $\alpha(z_0) = \beta(z_0) = -\tan^{-1}(a/b)$ from (A8). It follows that $\beta(z) \geqslant \alpha(z)$ for $z > z_0$, or $\beta(z) \leqslant \alpha(z)$ for $z < z_0$ (see Theorem 1.3 in Teschl (2012)).

The function θ_α (or θ_β) vanishes when $\alpha = n\pi$ (or $\beta = n\pi$) for some integer n, and from (A11) (or (A12)) it is clear that α_z (or β_z) is positive at such locations. Let n_0 be

https://doi.org/10.1017/jfm.2026.11984 Published online by Cambridge University Press

the smallest integer such that $n_0\pi > \tan^{-1}(a/b)$. If $\theta_\alpha(z_1) = 0$ for some $z_1 > z_0$, then $\beta(z_1) \geqslant \alpha(z_1) \geqslant n_0\pi$, and it follows that $\beta(\hat{z}) = n_0\pi$ for some $\hat{z}$ in the interval $(z_0, z_1]$. An analogous argument shows that if $\theta_\alpha(z_1) = 0$ for some $z_1 < z_0$, then there is a $\hat{z} \in [z_1, z_0)$ such that $\theta_\beta(\hat{z}) = 0$.

If we make the further assumptions that $q_\alpha > 0$ in the interior of I, θ_β does not vanish in the interior of I, and $\theta_{\beta z}(z_s) = 0$ for some $z_s \in I$. Then $\theta_{\alpha z}(z_s)$ either has the same sign as $\theta_{\alpha z}(z_0)$, or $\theta_{\alpha z}(z_s) = 0$. To show this, assume again that $z_s > z_0$. Note that $\theta_{\alpha z} = 0$ (or $\theta_{\beta z} = 0$) corresponds to $\alpha = (n - 1/2)\pi$ (or $\beta = (n - 1/2)\pi$) for some integer n. With $q_\beta \geqslant q_\alpha > 0$, it also follows that α is an increasing function of z. Since θ_β does not vanish in the interior of I and θ_β and θ_α are increasing functions of z, it follows that $\beta(z_s) = (n_0 - 1/2)\pi \geqslant \alpha(z_s) \geqslant \tan^{-1}(a/b) > (n_0 - 3/2)\pi$, n_0 again being the smallest integer such that $n_0\pi > \tan^{-1}(a/b)$. Therefore $\theta_{\alpha z}(z_s) = \cos(\alpha(z_s))/p_\alpha(z_s)$ either vanishes if $\alpha(z_s) = (n_0 - 1/2)\pi$, or has the same sign as $\theta_{\alpha z}(z_0) = \cos(\tan^{-1}(a/b))/p_\alpha(z_0)$. An analogous argument leads to the same result if $z_s < z_0$. □

Consider then the solution of the Sturm–Liouville problem (4.19) corresponding to the largest eigenvalue σ as the comparison function θ_β. By the Sturm oscillation theorem, this solution has no zeros inside the domain, and satisfies a problem of the form in (A7) with $p_\beta = 1$ and $q_\beta = F_T\bar{\tau} - \sigma$. The functions ϕ_1 and ϕ_2 also satisfy (A7) for θ_α, with $p_\alpha = 1$ and $q_\alpha = F_T\bar{\tau} \leqslant q_\beta$, for either $z_0 = H$ for ϕ_1 or $z_0 = 0$ for ϕ_2.

It follows from the modified Sturm–Picone theorem that ϕ_1 and ϕ_2 have no zeros and hence do not change sign in $(0, H)$. For ϕ_2, the boundary condition at $z = H$ immediately shows that ϕ_2 is therefore positive in $(0, H)$ and hence in $[0, H)$ (since ϕ_2 cannot vanish and have vanishing gradient at $z = 0$). To show that ϕ_1 is negative in $[0, H)$, we appeal to the gradient result in the modified Sturm–Picone theorem, which shows that $\phi_{1,z}(H) > 0$ as $\phi_{1,z}(0) > 0$. Combined with $\phi_1(H) = 0$, it follows that $\phi_1 < 0$ on $[0, H)$.

We have just established that $\Theta_H > 0$ on the first and third branches. Similarly, we can show that $\Theta_s > 0$ under the same conditions, and that Q_H is then positive. In particular, differentiating (3.2) and (3.3) with respect to s leads to the boundary value problem

$$-\Theta_{s,zz} = F_T\bar{\tau}\Theta_s + (F_\tau\bar{\tau} + F)(H - z), \quad \Theta_{s,z}(0) = 0, \quad \Theta_s(H) = 0, \tag{A13}$$

with solution

$$\Theta_s(z) = \int_0^H G(z, z')\left[F_\tau(z')\,\bar{\tau}(z') + F(z')\right](H - z')\,\mathrm{d}z'. \tag{A14}$$

Since G and the inhomogeneous term are positive, so is Θ_s.

To show that Q_H is positive, we can use the following: first, we have

$$U_{H,z} = F_\tau s + F_T\Theta_H, \tag{A15}$$

subject to $U_H = 0$ at $z = 0$, this ensures that $U_H > 0$, and

$$Q_H = \int_0^H U_H\,\mathrm{d}z + U(H) \tag{A16}$$

then leads to $Q_H > 0$. At this point, we can conclude that

$$\mathrm{Im}\left[\theta_{\frac{1}{2}}(z)/\eta\right] = \mathrm{Im}\left[K\sqrt{\frac{\sigma_0}{\kappa}}\theta_0(0)/\eta\right]\phi_1(z) = -K\sqrt{\frac{Q_H}{2\kappa}}\Theta_H(0)\phi_1(z) > 0. \tag{A17}$$

https://doi.org/10.1017/jfm.2026.11984 Published online by Cambridge University Press

Appendix B. Joseph's bounds on multiple base-flow solutions

Consider

$$\Theta_{\zeta\zeta} + s^{n+1} H^{n+3} \zeta^{n+1} \mathcal{E}(\Theta) = 0, \quad \Theta(\zeta = 0) = 0, \quad \Theta_\zeta(\zeta = 1) = \Gamma H, \tag{B1}$$

where $F(\bar{\tau}, \Theta) = \bar{\tau}^n \mathcal{E}(\Theta)$ and $\zeta = 1 - (z/H)$. The homogenised version of this problem uses the variable $\psi = \Theta - \Gamma H \zeta$, which is non-negative.

Joseph's comparison function $\phi(\zeta)$ solves the problem

$$\phi_{\zeta\zeta} + S^{n+1} H^{n+3} \zeta^{n+1} \phi = 0, \quad \phi(0) = \phi_\zeta(1) = 0. \tag{B2}$$

The solution is

$$\phi = \sqrt{\zeta} J_\nu\big(\omega \zeta^{\frac{n+3}{2}}\big), \quad \nu = \tfrac{1}{n+3}, \quad \omega = \frac{2 S^{\frac{n+1}{2}} H^{\frac{n+3}{2}}}{n+3}, \tag{B3}$$

where J_ν is the usual Bessel function of the first kind and ω is the first zero of ϕ_ζ; i.e.

$$J_\nu(\omega) + (n+3)\omega J_\nu'(\omega) = 0, \tag{B4}$$

which gives $\omega \approx 0.849$ for $n = 3$.

Standard machinations give

$$0 = \int_0^1 (\psi \phi_{\zeta\zeta} - \phi \Theta_{\zeta\zeta})\, \mathrm{d}\zeta = H^{n+3} \int_0^1 [s^{n+1} \mathcal{E}(\Theta) - S^{n+1} \psi] \phi \zeta^{n+1} \mathrm{d}\zeta. \tag{B5}$$

That is,

$$\frac{s^{n+1}}{S^{n+1}} = \frac{\int_0^1 \psi \phi \zeta^{n+1} \mathrm{d}\zeta}{\int_0^1 \phi \mathcal{E}(\Theta) \zeta^{n+1} \mathrm{d}\zeta} = \left\{ 1 + \frac{\int_0^1 [\mathcal{E}(\Theta) - \psi] \phi \zeta^{n+1} \mathrm{d}\zeta}{\int_0^1 \psi \phi \zeta^{n+1} \mathrm{d}\zeta} \right\}^{-1}. \tag{B6}$$

To furnish a bound, we take out the smallest value of $\mathcal{E}(\Theta) - \psi = \mathcal{E}(\Theta) - \Theta + \Gamma H \zeta$ from $\int_0^1 [\mathcal{E}(\Theta) - \psi] \phi \zeta^{n+1} \mathrm{d}\zeta$ (assuming that this is positive) and the largest value of $\psi = \Theta - \Gamma H \zeta$ from $\int_0^1 \psi \phi \zeta^{n+1} \mathrm{d}\zeta$. In other words,

$$s^{n+1} \leqslant S^{n+1} \left\{ 1 + \frac{\min[\mathcal{E}(\Theta) - \Theta]}{\max[\Theta - \Gamma H \zeta]} \right\}^{-1}, \tag{B7}$$

where we can replace the factor S^{n+1} with $(1/4)(n+3)^2 \omega^2 H^{-n-3}$.

For the Frank-Kamenetskii approximation ($\mathcal{E}(\Theta) = e^\Theta$), the previous inequality can be written as

$$s^{n+1} \leqslant S^{n+1} \frac{\Theta(\zeta = 1) - \Gamma H}{\Theta(\zeta = 1) - \Gamma H + 1}. \tag{B8}$$

On the other hand, using the Arrhenius relation ($\mathcal{E}(\Theta) = e^{\Theta/(1+\delta\Theta)}$), the assumption that $\mathcal{E}(\Theta) - \psi > 0$ is violated for sufficiently large values of the base temperature.

Appendix C. Large base-temperature asymptotics

The base flow satisfies

$$\Theta_{zz} = -s^{n+1} (H - z)^{n+1} \exp\left(\frac{\Theta}{1 + \delta\Theta} \right), \quad \Theta(H) = 0, \quad \Theta_z(0) = -\Gamma. \tag{C1}$$

https://doi.org/10.1017/jfm.2026.11984 Published online by Cambridge University Press

For $\Theta(0) = T_0 \gg 1$ and $\delta T_0 = O(1)$, the viscous heating term becomes exponentially large at the base of the flow, demanding the presence of a boundary layer with a thickness of order $(sH)^{-(1/2)(n+1)} e^{-(1/2)T_0} \ll 1$. Within that layer, we can approximate the factor $(H-z)^{n+1}$ in (C1) by H^{n+1} and discard the geothermal heat flux Γ. Thus $\Theta \sim T_0 + \Theta^*$, where

$$\Theta^*_{zz} = -s^{n+1} H^{n+1} \exp\left(\frac{T_0}{1+\delta T_0} + \frac{\Theta^*}{(1+\delta T_0)^2}\right), \quad \Theta^*(H) = 0, \quad \Theta^*_z(0) = 0, \tag{C2}$$

which can be solved, yielding

$$\Theta \sim T_0 + (1+\delta T_0)^2 \ln\left[\operatorname{sech}^2\left(z\sqrt{\frac{(sH)^{n+1}\exp\left(T_0/(1+\delta T_0)\right)}{2(1+\delta T_0)^2}}\right)\right], \tag{C3}$$

with $z\sqrt{(1/2)(sH)^{n+1}e^{T_0}} = O(1)$. This solution has the limit

$$\Theta \sim T_0 - z\sqrt{2(1+\delta T_0)^2 (sH)^{n+1} \exp\left(\frac{T_0}{1+\delta T_0}\right)}, \tag{C4}$$

as we ascend into the region above the boundary layer. There, the viscous heating term switches off exponentially quickly, leaving a linear temperature profile that must be matched with (C4). Finally, demanding that $\Theta(H) = 0$ implies that

$$T_0 \sim H\sqrt{2(1+\delta T_0)^2 (sH)^{n+1} e^{\frac{T_0}{1+\delta T_0}}}, \quad \text{or} \quad s^{n+1} \sim \frac{T_0^2 e^{-\frac{T_0}{1+\delta T_0}}}{2(1+\delta T_0)^2 H^{n+3}}. \tag{C5}$$

Appendix D. Non-uniform steady states and trajectories in (s, H, Q)-space

In this appendix we briefly describe a steady state that is non-uniform in the streamwise direction. We assume a flat bed and a prescribed accumulation/ablation rate $a = a(x)$. In addition, we take the Péclet number to be zero, so that temperature advection is neglected. Terrestrial ice sheets typically do not have small enough Péclet numbers to make this realistic, but the model remains conceptually useful in illustrating the link between our results for a parallel-sided slab in §§ 3–4: in the steady state computed here, each vertical ice column is governed by the same slab problem as in the uniform base state, now driven by the local slope $s = -h^*_x$.

Let the non-uniform steady state be denoted by $h = h^*(x)$, $u = u^*(x, z)$, $T = T^*(x, z)$, $\tau = \tau^*(x, z)$ and $Q = Q^*(x)$. The governing equations are (see also Fowler (1992))

$$-T^*_{zz} = \tau^* f(T^*, \tau^*), \quad \tau^* = -h^*_x(h^* - z), \quad u^*_z = \operatorname{sgn}(\tau^*)\, f(T^*, \tau^*), \tag{D1}$$

with flux

$$Q^*(x) = \int_0^{h^*(x)} u^*(x, z)\,\mathrm{d}z = \int_0^{h^*(x)} (h^* - z)\ \operatorname{sgn}(\tau^*)\ f(T^*, \tau^*)\,\mathrm{d}z. \tag{D2}$$

These are supplemented by

$$Q^*_x = a(x), \quad T^* = 0 \quad \text{at } z = h^*(x), \quad T^*_z = -\Gamma \quad \text{and} \quad u^* = 0 \quad \text{at } z = 0, \tag{D3}$$

where a is a source term (referred to as surface mass balance in glaciology) that represents snowfall (if $a > 0$) or melting (if $a < 0$), which is omitted in (2.6). In what follows, we also restrict ourselves to the constitutive relation (2.24).

https://doi.org/10.1017/jfm.2026.11984 Published online by Cambridge University Press

We assume a to be an even function that is positive at the origin and decreases monotonically for $x > 0$. We can therefore assume symmetry around $x = 0$ (the ice divide), with

$$Q(x) = \int_0^x a(x)\,\mathrm{d}x \tag{D4}$$

and an ice margin at $x = x_c$ where

$$Q(x_c) = \int_0^{x_c} a(x)\,\mathrm{d}x = 0. \tag{D5}$$

We assume that ice thickness $h(x_c)$ vanishes here. Since a is monotonically decreasing, we are guaranteed $Q > 0$ for $x \in (0, x_c)$, so that $h_x^* < 0$ and $\tau^* > 0$ for $x \in (0, x_c)$, and (D2) reduces to

$$Q^*(x) = \int_0^{h^*(x)} (h^* - z)^{n+1}(-h_x^*)^n \exp\left(\frac{T^*}{1+\delta T^*}\right)\mathrm{d}z. \tag{D6}$$

At the margin, we can expect the slope h_x^* to become singular (Fowler 1992). To remove that singularity, we introduce a change of variable (see also Calvo *et al.* (2003) and Schoof (2003))

$$q = (h^*)^{\frac{2(n+1)}{n}}, \quad \zeta = \frac{z}{h^*(x)} = \frac{z}{q(x)^{\frac{n}{2(n+1)}}}. \tag{D7}$$

Then, from (D6)

$$\begin{aligned} Q^*(x) &= \frac{n^n(-q_x)^n}{2^n(n+1)^n}\int_0^1 (1-\zeta)^{n+1}\exp\left(\frac{T^*}{1+\delta T^*}\right)\mathrm{d}\zeta \\ &\geqslant \frac{n^n(-q_x)^n}{2^n(n+1)^n}\int_0^1 (1-\zeta)^{n+1}\,\mathrm{d}\zeta = \frac{n^n(-q_x)^n}{2^n(n+1)^n(n+2)} \geqslant 0, \end{aligned} \tag{D8}$$

where we have used the fact that $T(z) \geqslant T(h)$ for a solution of (D1) and (D3), and that $q_x = (2(n+1)/n)(h^*)^{(2+n)/n}h_x^*$. Since $Q^*(x) = \int_x^{x_c} a(x')\,\mathrm{d}x'$, it follows that $q_x \to 0$ as $x \to x_c$, alleviating the singularity in h_x^*.

Moreover, after the transformation (D7), the temperature problem (D1), (D3) becomes

$$-T_{\zeta\zeta}^* = \left(\frac{n}{2n+2}\right)^{n+1} q^{-1/(n+1)}(-q_x)^{n+1}(1-\zeta)^{n+1}\exp\left(\frac{T^*}{1+\delta T^*}\right) \tag{D9}$$

for $0 < \zeta < 1$, with $T^* = 0$ at $\zeta = 1$ and $T_\zeta^* = -q^{n/(2n+2)}\Gamma$ at $\zeta = 0$. If we wish to decipher the local behaviour near the margin, then the remaining issue is the size of the coefficient $\alpha^* = q^{-1/(n+1)}(-q_x)^{n+1}$ as $x \to x_c$. It is self-consistent to assume that $\alpha^* \to 0$, since then $T^* = O(\alpha^*)$ and the first line of (D8) becomes $Q(x) \sim |a(x_c)|(x_c - x) \sim ((n^n(-q_x)^n)/(2^n(n+1)^n(n+2)))$ so

$$\begin{aligned} -q_x &\sim \frac{2(n+1)}{n}|(n+2)a(x_c)|^{1/n}(x_c - x)^{1/n}, \\ q &\sim 2|(n+2)a(x_c)|^{1/n}(x_c - x)^{(n+1)/n}, \end{aligned} \tag{D10}$$

which agrees with the assumption that $\alpha^* = q^{-1/(n+1)}(-q_x)^{n+1} \to 0$: physically, despite the infinite slope near the margin, the small ice thickness (and near-vanishing flux) ensures small enough dissipation and sufficiently rapid conduction that the temperature in the ice

https://doi.org/10.1017/jfm.2026.11984 Published online by Cambridge University Press

is set entirely by the surface, and the solution follows branch 1 of the flux–thickness–slope relationship described in § 3.2. There does not appear to be an alternative local solution near the margin, though to rigorously exclude one would require $q(x)$ to be bounded below *a priori* in terms of $-q_x(x)$ near x_c, which we have not been able to do.

Away from the margin, we return to the full problem (D1)–(D3). At each x, the z-problem is exactly the base-flow problem studied in the main text, now with local slope $s = -h^*_x$, thickness $H = h^*$ and flux $Q = Q^*$. As shown in § 3.2 and figure 4, s is then uniquely determined by H and Q, so the steady profile reduces to a nonlinear first-order equation for $h^*(x)$, which can be solved numerically. Equivalently, each ice column defines a point

$$(-h^*_x,\, h^*,\, Q^*) \tag{D11}$$

in (s, H, Q)-space, and as x varies these points trace a trajectory on the previously computed surface in figure 4. Plotting this trajectory provides a convenient way to diagnose the non-uniform steady state and, in particular, to determine whether and where it approaches the fold or enters branch 2.

References

ALLEY, R.B. & BINDSCHADLER, R.A. (eds.) 2001 *The West Antarctic Ice Sheet: Behaviour and Environment*. American Geophysical Union.

BARTELS, S. 2015 *The Allen–Cahn Equation*, pp. 153–182. Springer International Publishing.

BRINKERHOFF, D.J. & JOHNSON, J.V. 2015 Dynamics of thermally induced ice streams simulated with a higher-order model. *J. Geophys. Res. Earth Surf.* **120**, 1743–1770.

CALVO, N., DÍAZ, J.I., DURANY, J., SCHIAVI, E. & VÁZQUEZ, C. 2003 On a doubly nonlinear parabolic obstacle problem modelling ice sheet dynamics. *SIAM J. Appl. Math.* **63** (2), 683–707.

CLARKE, G.K.C. 1976 Thermal regulation of glacier surging. *J. Glaciol.* **16** (74), 231–250.

CLARKE, G.K.C., NITSAN, U. & PATERSON, W.S.B. 1977 Strain heating and creep instability in glaciers and ice sheets. *Rev. Geophys.* **15** (2), 235–247.

CUFFEY, K.M. & PATERSON, W.S.B. 2010 *The Physics of Glaciers*. 4th edn. Elsevier.

FOWLER, A.C. 1980 The existence of multiple steady states in the flow of large ice masses. *J. Glaciol.* **25** (91), 183–184.

FOWLER, A.C. 1992 Modelling ice sheet dynamics. *Geophys. Astrophys. Fluid Dyn.* **63** (1–4), 29–65.

FOWLER, A.C. 1997 Glaciers and ice sheets. In *The Mathematics of Models for Climatology and Environment* (ed. J.I. DÍAZ), pp. 301–336. Springer.

FOWLER, A.C. & LARSON, D.A. 1978 On the flow of polythermal glaciers – I. Model and preliminary analysis. *Proc. R. Soc. Lond. Ser. A Math. Phys. Sci.* **363**, 217–242.

FOWLER, A.C. & LARSON, D.A. 1980 Thermal stability properties of a model of glacier flow. *Geophys. J. Intl* **63** (2), 347–359.

FOWLER, A.C., MURRAY, T. & NG, F.S.L. 2001 Thermally controlled glacier surging. *J. Glaciol.* **47** (159), 527–538.

HELFRICH, K.R. 1995 Thermo-viscous fingering of flow in a thin gap: a model of magma flow in dikes and fissures. *J. Fluid Mech.* **305**, 219–238.

HINDMARSH, R.C.A. 2004 Thermoviscous stability of ice-sheet flows. *J. Fluid Mech.* **502**, 17–40.

HINDMARSH, R.C.A. 2009 Consistent generation of ice-streams via thermo-viscous instabilities modulated by membrane stresses. *Geophys. Res. Lett.* **36** (6), L06502.

HINDMARSH, R.C.A. 2011 Ill-posedness of the shallow-ice approximation when modelling thermo-viscous instabilities. *J. Glaciol.* **57** (206), 1177–1178.

HUTTER, K. 1983 *Theoretical Glaciology: Material Science of Ice and the Mechanics of Glaciers and Ice Sheets, Mathematical Approaches to Geophysics*, vol. 1. Springer.

JOSEPH, D.D. 1964 Variable viscosity effects on the flow and stability of flow in channels and pipes. *Phys. Fluids* **7** (11), 1761–1771.

JOSEPH, D.D. 1965*a* Non-linear heat generation and stability of the temperature distribution in conducting solids. *Intl J. Heat Mass Transfer* **8** (2), 281–288.

JOSEPH, D.D. 1965*b* Stability of frictionally-heated flow. *Phys. Fluids* **8** (12), 2195–2200.

JOSEPH, D.D. 1966 Bounds on λ for positive solutions of $\Delta\psi + \lambda f(r)\{\psi + G(\psi)\} = 0$. *Q. Appl. Math.* **23** (4), 349–354.

https://doi.org/10.1017/jfm.2026.11984 Published online by Cambridge University Press

KAMB, B., RAYMOND, C.F., HARRISON, W.D., ENGELHARDT, H., ECHELMEYER, K.A., HUMPHREY, N., BRUGMAN, M.M. & PFEFFER, T. 1985 Glacier surge mechanism: 1982-1983 surge of Variegated Glacier, Alaska. *Science* **227** (4686), 469–479.

KYRKE-SMITH, T.M., KATZ, R.F. & FOWLER, A.C. 2014 Subglacial hydrology and the formation of ice streams. *Proc. R. Soc. Lond. A* **470**, 20130494.

MADDOCKS, J.H. 1987 Stability and folds. *Arch. Rat. Mech. Anal.* **99**, 301–328.

MANTELLI, E., HASELOFF, M. & SCHOOF, C. 2019 Ice sheet flow with thermally activated sliding. Part 1: the role of advection. *Proc. R. Soc. A: Math. Phys. Engng Sci.* **475** (2230), 20190410.

MANTELLI, E. & SCHOOF, C. 2019 Ice sheet flow with thermally activated sliding. Part 2: the stability of subtemperate regions. *Proc. R. Soc. A: Math. Phys. Engng Sci.* **475** (2231), 20190411.

MURRAY, T., STROZZI, T., LUCKMAN, A., JISKOOT, H. & CHRISTAKOS, P. 2003 Is there a single surge mechanism? Contrasts in dynamics between glacier surges in Svalbard and other regions. *J. Geophys. Res.: Solid Earth* **108** (B5), 2237.

PAYNE, A.J., *et al.* 2000 Results from the EISMINT model intercomparison: the effects of thermomechanical coupling. *J. Glaciol.* **46** (153), 227–238.

PAYNE, A.J. 1995 Limit cycles in the basal thermal regime of ice sheets. *J. Geophys. Res.: Solid Earth* **100** (B3), 4249–4263.

PAYNE, A.J. & BALDWIN, D.J. 2000 Analysis of ice-flow instabilities identified in the EISMINT intercomparison exercise. *Ann. Glaciol.* **30**, 204–210.

ROBIN, G.DE Q. 1955 Ice movement and temperature distribution in glaciers and ice sheets. *J. Glaciol.* **2** (18), 523–532.

SAITO, F., ABE-OUCHI, A. & BLATTER, H. 2006 European Ice Sheet Modelling Initiative (EISMINT) model intercomparison experiments with first-order mechanics. *J. Geophys. Res.: Earth Surface* **111** (F2), F02012.

SCHOOF, C. 2003 The effect of basal topography on ice sheet dynamics. *Contin. Mech. Thermodyn.* **15** (3), 295–307.

SCHOOF, C. & HEWITT, I. 2013 Ice-sheet dynamics. *Annu. Rev. Fluid Mech.* **45**, 217–239.

SCHOOF, C. & HINDMARSH, R.C.A. 2010 Thin-film flows with wall slip: an asymptotic analysis of higher order glacier flow models. *Quart. J. Mech. Appl. Math.* **63** (1), 73–114.

SCHOOF, C. & MANTELLI, E. 2021 The role of sliding in ice stream formation. *Proc. R. Soc. A: Math. Phys. Engng Sci.* **477** (2248), 20200870.

TESCHL, G. 2012 *Ordinary Differential Equations and Dynamical Systems, Graduate Studies in Mathematics*, vol. 140. American Mathematical Society.

YUEN, D.A. & SCHUBERT, G. 1979 The role of shear heating in the dynamics of large ice masses. *J. Glaciol.* **24** (90), 195–212.

ZETTL, A. 2005 *Sturm–Liouville Theory Mathematical Surveys and Monographs*, vol. 121. American Mathematical Society.

https://doi.org/10.1017/jfm.2026.11984 Published online by Cambridge University Press